nature communications

Article

https://doi.org/10.1038/s41467-025-60978-w

An O-glycopeptide participates in the formation of distinct $A\beta_{42}$ fibril structures and attenuates $A\beta_{42}$ neurotoxicity

Received: 30 September 2024

Accepted: 9 June 2025

Published online: 01 July 2025

Check for updates

Qijia Wei[1,2,3,11], Dangliang Liu[1,2,3,11], Wencheng Xia[4,5,11], Fengzhang Wang[6,11], Lu Huang[1,2,3], Jun Zhang[1,2,3], Xiaoya Wang[1,3], Zhongxin Xu[1,2,3], Changdong He[1,2,3], Wenzhe Li[1], Xiaomeng Shi[1], Chu Wang[6,7], Yuan Liu[6] ✉, Cong Liu[4,8,9] ✉ & Suwei Dong[1,2,3,10] ✉

The self-assembly of biomolecules through noncovalent interactions is critical in both physiological and pathological processes, as exemplified by the assembly of amyloid β peptide (Aβ) into oligomers or fibrils in Alzheimer's disease (AD). Developing molecules that can modulate this assembly process holds significant mechanistic and therapeutic potential. In this study, we identified glycopeptides as a class of protein aggregation modulators, showing that β-*N*-acetylgalactosamine (β-GalNAc)-modified $A\beta_{9\text{-}21}$ promotes $A\beta_{42}$ fibrillation while reducing its toxic oligomers. Using biochemical assays, cryo-EM, and molecular dynamics simulations, we demonstrated that β-GalNAc-modified $A\beta_{9\text{-}21}$ coassembles with $A\beta_{42}$, forming unique fibril structures stabilized by both hydrophobic interactions and an organized hydrogen bond network facilitated by the glycopeptide. Importantly, β-GalNAc-modified $A\beta_{9\text{-}21}$ can alleviate the neurotoxicity of $A\beta_{42}$ in neuronal cells and an AD male mouse model. These findings underscore the potential of glycopeptides in regulating amyloid aggregation and provide structural insights for designing molecules targeting amyloid-related pathologies.

In nature, the self-assembly process that builds up polymeric structures from repetitive monomers through noncovalent interactions plays important roles in various physiological and pathological activities, such as the construction of the cytoskeleton, trafficking of cellular cargo through the clathrin-mediated pathway, assembly of ribosomes as the protein production machinery, and the formation of pathological amyloid fibrils[1,2]. In particular, the assembly of aggregation-prone proteins is suggested to be closely related to the development of a wide range of neurodegenerative diseases[3]. For example, amyloid β peptide (Aβ) can assemble through hydrophobic interactions and form oligomers or fibrils, which are relevant to Alzheimer's disease, and the formation of α-synuclein fibrils is the hallmark of Parkinson's disease[4–6]. Because the extent or aggregation state of amyloid proteins is closely associated with their biological activities[4], an in-depth exploration of the assembly mechanism and corresponding

[1]State Key Laboratory of Natural and Biomimetic Drugs, Peking University, Beijing, China. [2]Chemical Biology Center, Peking University, Beijing, China. [3]Department of Chemical Biology, School of Pharmaceutical Sciences, Peking University, Beijing, China. [4]Interdisciplinary Research Center on Biology and Chemistry, State Key Laboratory of Chemical Biology, Shanghai Institute of Organic Chemistry, Chinese Academy of Sciences, Shanghai, China. [5]University of Chinese Academy of Sciences, Shijingshan District, Beijing, China. [6]College of Chemistry and Molecular Engineering, Peking University, Beijing, China. [7]Peking-Tsinghua Center for Life Sciences, Academy for Advanced Interdisciplinary Studies, Peking University, Beijing, China. [8]Shanghai Academy of Natural Sciences (SANS), Fudan University, Shanghai, China. [9]Shanghai Key Laboratory of Aging Studies, Shanghai, China. [10]Ningbo Institute of Marine Medicine, Peking University, Ningbo, China. [11]These authors contributed equally: Qijia Wei, Dangliang Liu, Wencheng Xia, Fengzhang Wang.
✉e-mail: wendao@pku.edu.cn; liulab@sioc.ac.cn; dongsw@pku.edu.cn

regulatory factors is urgently needed to understand related neurodegenerative diseases.

The aggregation state of fibrillation-prone proteins can be influenced by different factors, including humoral conditions (pH and the concentration of metal ions)[7,8] and posttranslational modifications (PTMs) of protein monomers[9]. Moreover, various endogenous or exogenous aggregation modulators have been explored for their ability to intervene in the assembly process of amyloid proteins[10]. For example, early results showed that small molecules such as carvedilol and lovastatin could interrupt the aggregation process of Aβ and block the formation of typical β-sheet secondary structures[10]; the pincer-like europium(III) complex (EC) could interact with the oligomeric form of Aβ and promote its aggregation[11]. Supramolecular nanostructures have also been found to accelerate the aggregation of human islet amyloid polypeptide (IAPP), while mitigating its associated toxicity[12]. In addition to small molecules and nanomaterials[13], peptide modulators have attracted the attention of researchers because of their ideal biocompatibility, high specificity, and relatively low cost. The core fragments of aggregating proteins, particularly those that contribute primarily to self-assembly, inspire numerous studies on developing peptide derivatives that can interrupt aggregation. For example, the hydrophobic core (KLVFF) and C-terminal fragments (VVIA) of Aβ and the derived peptides are able to inhibit Aβ aggregation (Fig. 1)[14]. The tau-derived hexapeptide motif VQIVYK and its β-O-linked glycosylated variants have been reported to attenuate the aggregation of the tau-derived model peptide[15]; peptides derived from the α-syn$_{68\text{-}77}$ stretch can block the elongation of the α-synuclein fibril[16]. Notably, most developed peptide modulators are inhibitors of protein aggregation, whereas few examples[12,17–20] have shown the ability to promote the aggregation process. Moreover, illustrating the molecular mechanism of the effectors involved in the aggregation process remains a daunting challenge[13,21], which significantly limits the understanding and application of these aggregation modulators for research and therapeutic development.

Considering recent research revealing that the oligomeric forms of some amyloid proteins could be more toxic toward neurons[22,23], further investigation of structures for modulating amyloid protein assembly and clarification of the underlying molecular mechanism would be extremely valuable. Inspired by protein glycosylation, a posttranslational modification that can regulate both the aggregation states and biological activities of amyloid proteins (such as Aβ, α-synuclein, and tau proteins)[24–26] and modulate self-assembly of peptides or proteins[27,28], the introduction of a glycan to a fragment of amyloid protein influences the aggregation process.

In this study, we synthesized a series of glycopeptides based on the central hydrophobic core of Aβ and investigated their modulatory effects on Aβ aggregation. Notably, among the six synthetic variants of Aβ$_{9\text{-}21}$ appending different O-glycans at the tyrosine site, β-GalNAc-modified Aβ$_{9\text{-}21}$ (**4b**) significantly accelerated the aggregation process of Aβ$_{42}$. We showed that glycopeptide **4b** coassembled with Aβ$_{42}$ to promote rapid fibril formation. Importantly, by using cryo-EM, we further revealed that **4b** may directly interact with Glu11-Val18 of Aβ$_{42}$ to cooperatively form three different structural polymorphs of coassembled fibrils with distinctive fibril core structures. Subsequent Rosetta modeling and molecular dynamics (MD) simulations of glycopeptide-Aβ$_{42}$ complexes suggested that hydrogen bonding network-enabled stabilization is crucial for the aggregation-promoting effect of glycopeptide **4b**. In conjunction with the neurotoxicity-alleviating effect of **4b** in SH-SY5Y cells and in an AD mouse model, these studies demonstrated the ability of glycosylation to increase the aggregation-promoting effect of an amyloid protein fragment, revealed a structural basis for mechanistic insight, and provided potential clues for designing glycopeptides to intervene in aggregation-prone protein-related pathological processes.

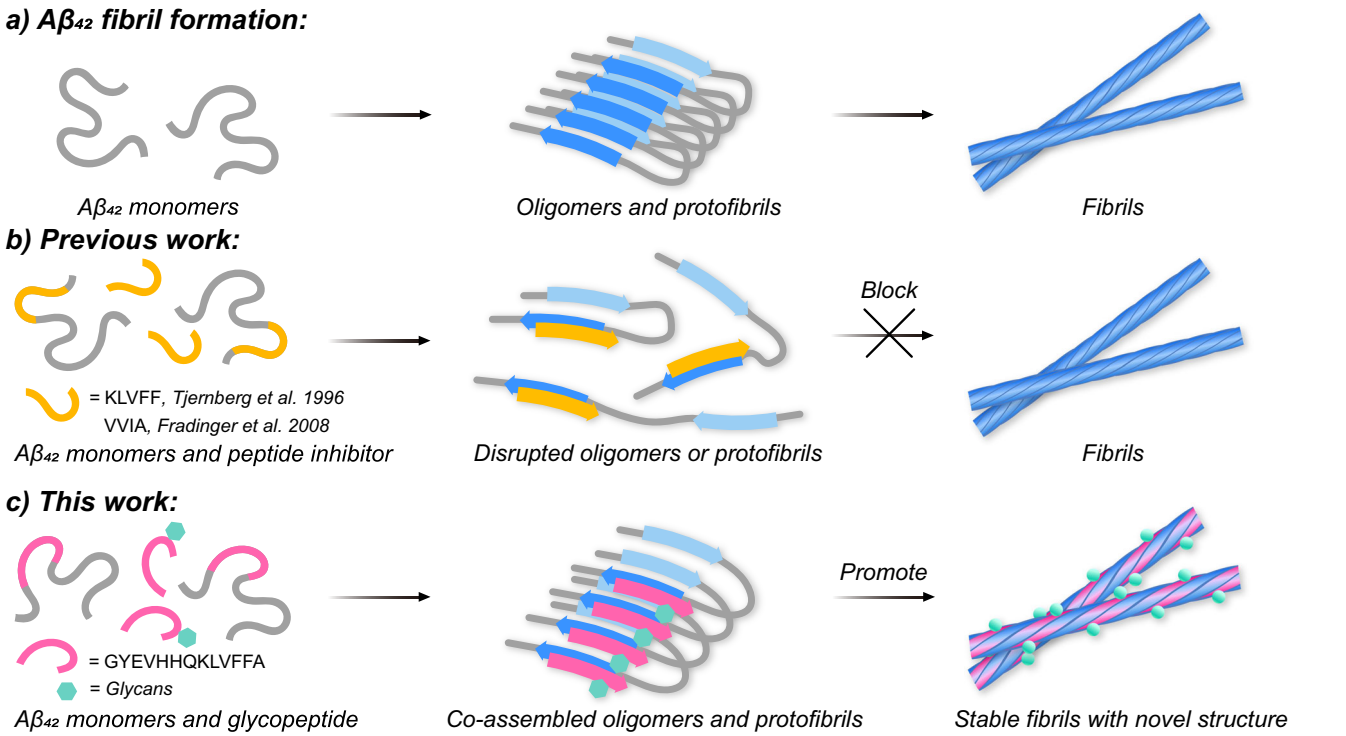

Fig. 1 | Self-assembly of Aβ$_{42}$ and representative modulators of the assembly process. a Schematic illustration of Aβ$_{42}$ self-assembly into oligomers and fibrils. **b** Representative molecules previously reported to inhibit Aβ$_{42}$ oligomerization and fibrillization. **c** Glycopeptides identified in this study that coassemble with Aβ$_{42}$ to form stable, structurally distinct fibrils.

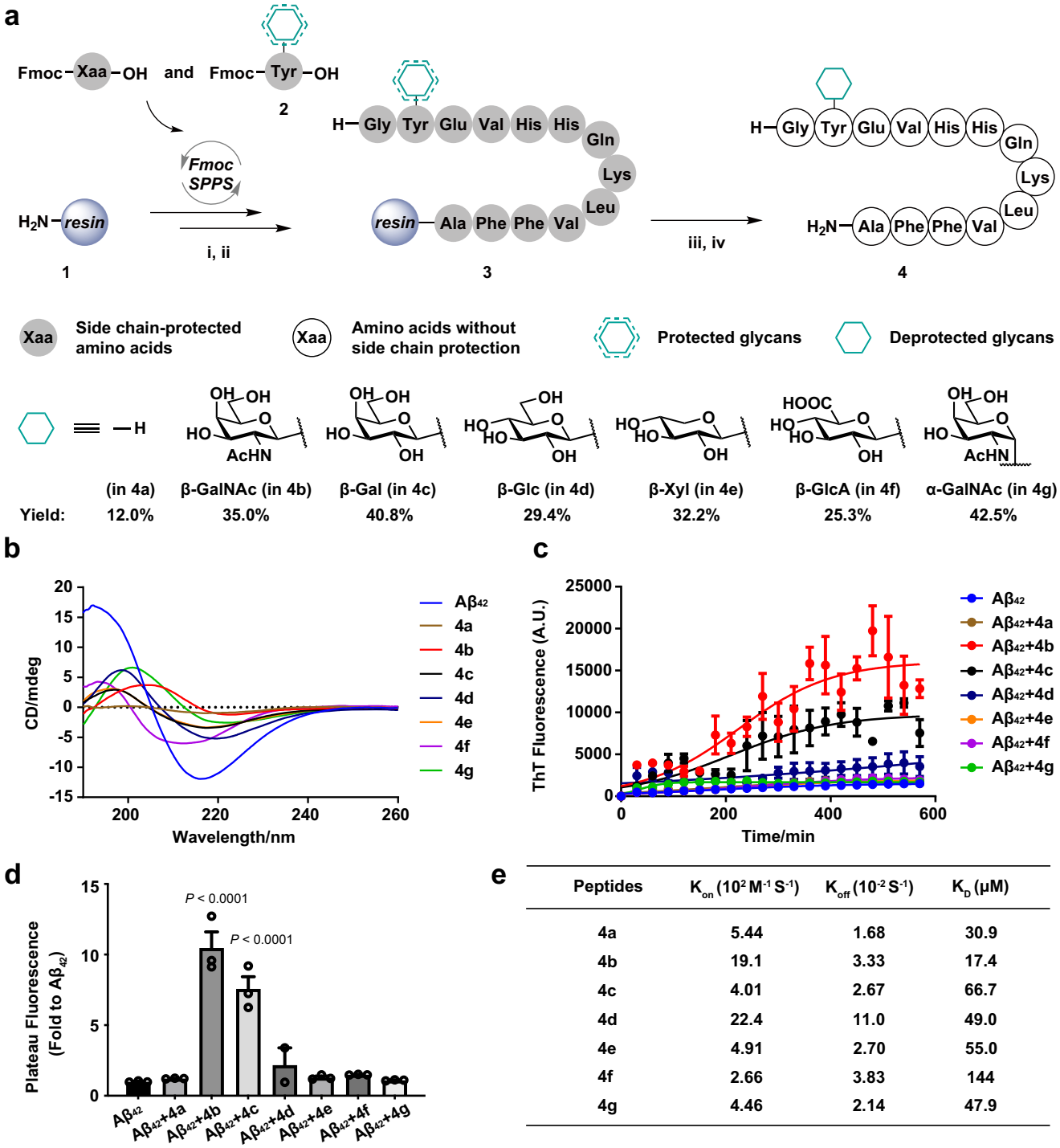

e

Peptides	K_{on} (10^2 M^{-1} S^{-1})	K_{off} (10^{-2} S^{-1})	K_D (μM)
4a	5.44	1.68	30.9
4b	19.1	3.33	17.4
4c	4.01	2.67	66.7
4d	22.4	11.0	49.0
4e	4.91	2.70	55.0
4f	2.66	3.83	144
4g	4.46	2.14	47.9

Fig. 2 | The glycoform and the stereochemistry of the glycosidic bond on $Aβ_{9-21}$ influence its interaction with $Aβ_{42}$. a Synthesis of glycosylated $Aβ_{9-21}$. Reaction conditions: (i) microwave-assisted Fmoc-SPPS; (ii) **2**, HATU, HOAt, DIEA, rt, 2 h×2; (iii) TFA/H_2O/TIPS (95:2.5:2.5), rt, 2 h; (iv) 1 M NaOH, 1 h. (b) Circular dichroism (CD) spectra of $Aβ_{42}$ and glycosylated $Aβ_{9-21}$ (n = 3). The values are the means. **c** Thioflavin T (ThT) analysis of the aggregation processes of $Aβ_{42}$ (6 μM) incubated with or without (glycosylated) $Aβ_{9-21}$ (12 μM). **d** Plateau fluorescence calculated from the ThT kinetic curves in (**c**) ($n = 3$). **e** The binding affinity of (glycosylated) $Aβ_{9-21}$ with $Aβ_{42}$ measured by BLI. Statistical significance was assessed using one-way ANOVA test. All values are presented as the means ± s.e.m.s. Source data are provided as a Source Data file.

Results

Design and synthesis of Tyr-O-glycosylated $Aβ_{9-21}$ peptides and evaluation of their regulatory effects on $Aβ_{42}$

KLVFF (peptide fragment $Aβ_{16-20}$) is widely recognized as the amyloid self-recognition segment and participates in the $Aβ_{42}$ aggregation process by forming a core β-sheet structure[29,30]. Within this region, the tyrosine 10 residue (Tyr_{10}) has been identified as a glycosylation site within Aβ fragment peptides in human cerebrospinal fluid, with a relatively high level in AD patients[31]. Our group previously demonstrated that O-Galβ1-3GalNAc modification on Tyr_{10} redirects $Aβ_{42}$ to form a new fibril polymorphic structure that is less stable[25]. We speculated that a Tyr-O-glycosylated Aβ fragment covering the KLVFF

https://doi.org/10.1038/s41467-025-60978-w

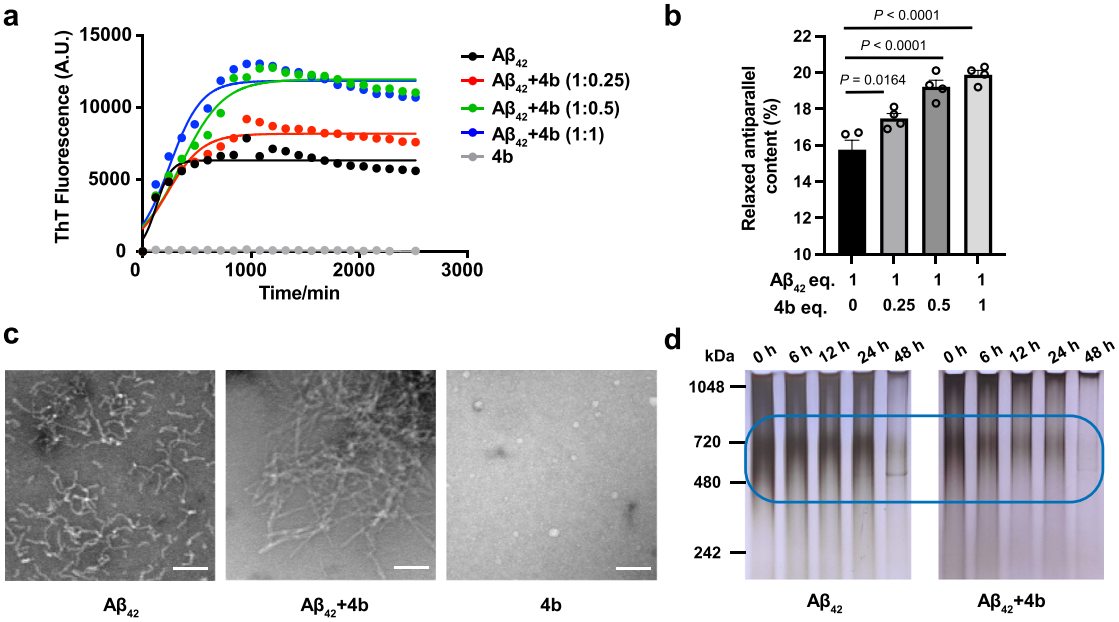

Fig. 3 | β-GalNAc Aβ$_{9-21}$ (4b) promoted Aβ$_{42}$ aggregation. a Thioflavin T (ThT) analysis of the aggregation processes of Aβ$_{42}$ (8 μM) incubated without or with different concentrations of **4b** ($n = 2$). **b** β-sheet content quantification (relaxed antiparallel content) based on circular dichroism (CD) spectra of Aβ$_{42}$ incubated without or with different concentrations of **4b** ($n = 3$). **c** Representative TEM images of **4b** and Aβ$_{42}$ incubated without or with **4b**. Scale bar, 100 nm. **d** Native-PAGE analysis of Aβ$_{42}$ incubated without or with **4b** for different durations (top). The ladder is shown on the left. The blue circles indicate high-molecular-weight soluble oligomers. Gel images reflect representative results from two independently performed experiments. Statistical significance was assessed using one-way ANOVA test. All values are presented as the means ± s.e.m.s. Source data are provided as a Source Data file.

region may be a lead sequence for discovering a innovative modulator of Aβ aggregation. Similarly, a native sequence, Aβ$_{9-21}$ (**4a**), and a range of glycosylated isoforms (**4b**-**4g**) were synthesized via a protocol analogous to that in a previous report[25]. Specifically, five different monosaccharides, namely, β-N-acetylgalactosamine (β-GalNAc, in **4b**), β-galactose (β-Gal, in **4c**), β-glucose (β-Glc, in **4d**), β-xylose (β-Xyl, in **4e**), and β-glucuronic acid (β-GluA, in **4f**), were introduced to the corresponding glycopeptide sequences. An α-GalNAc-modified peptide (**4g**) was also prepared to examine the possible influences of the stereochemistry of the glycosidic bond. All the peptides were obtained in decent yields and high purities via Fmoc-based solid-phase peptide synthesis (SPPS, Fig. 2a).

With these glycopeptides in hand, we first measured their secondary structures in solution with circular dichroism (Fig. 2b and Supplementary Table 1). The glycoform and stereochemistry of peptides enable them to have distinct secondary structures, and among the glycopeptides, β-GalNAc-modified Aβ$_{9-21}$ (**4b**) exhibited the greatest extent of antiparallel β-sheets. Then, we evaluated their ability to regulate Aβ$_{42}$ aggregation. The thioflavin T (ThT) fluorescence assay, which is widely used to quantify the content of β-sheet structures[32], was applied to monitor the aggregation process of Aβ$_{42}$ in the presence of different (glyco)peptides tested. Synthetic Aβ$_{42}$ peptide was pre-treated with ammonium hydroxide to form monomer, following a well-established protocol[33]. The Aβ$_{42}$ peptide alone aggregated with increasing time. However, in the presence of Aβ$_{9-21}$ (**4a**) and its glycosylated derivatives (**4b**-**4g**), the fluorescence intensity increased significantly and reached higher values within shorter periods. In particular, the addition of β-GalNAc-modified Aβ$_{9-21}$ (**4b**) had the most significant aggregation-promoting effect (Fig. 2c). Notably, fitting the curve with the sigmoidal equation revealed that, compared with Aβ$_{42}$ alone, the addition of glycopeptide **4b** increased the plateau intensity 10-fold, other Aβ$_{9-21}$ variants increased it 7.5-fold (Fig. 2d). Furthermore, the BLI results also demonstrated that glycopeptide **4b** has the highest binding affinity (17.9 μM) for Aβ$_{42}$ among peptides **4a**-**4g** (Fig. 2e and Supplementary Fig. 1). These results suggest that the glycans on Aβ$_{9-21}$ peptides influence their binding and interaction with Aβ$_{42}$, in which β-GalNAc modification enables Aβ$_{9-21}$ to have the strongest promotion effect on Aβ$_{42}$ aggregation.

β-GalNAc Aβ$_{9-21}$ promotes Aβ$_{42}$ fibrillation and decreases its oligomeric species

Given that glycopeptides can modulate Aβ$_{42}$ fibrillation, we further investigated the interaction between Aβ$_{42}$ and the one with the strongest promotion effect, β-GalNAc Aβ$_{9-21}$ (**4b**). When Aβ$_{42}$ was incubated with increasing concentrations of β-GalNAc Aβ$_{9-21}$, fluorescence intensity increased proportionally with the amount of **4b** (Fig. 3a). The addition of **4b** doubled the total amount of aggregated proteins (Supplementary Fig. 2a), although the aggregation rate was slower compared to Aβ$_{42}$ alone (Supplementary Fig. 2b, c). Interestingly, **4b** also promoted Aβ$_{40}$ aggregation, albeit to a lesser extent than Aβ$_{42}$ (Supplementary Fig. 2d–g). This observation is consistent with the slower nucleation rate of Aβ$_{40}$ in solution and its preference for nucleation on the surface of fibrils[34]. Furthermore, we incubated Aβ$_{42}$ monomers in PBS buffer with different amounts of glycopeptide **4b** for 24 h and analyzed their secondary structures via circular dichroism (CD). The CD spectra quantification results suggested that Aβ$_{42}$ possessed a greater β-sheet content when incubated with glycopeptide **4b** than when incubated alone (Fig. 3b). Specifically, the relaxed antiparallel β-sheet content increased from 15% to 20% as the relative ratio of **4b** increased from 0.25 to 1, confirming that glycopeptide **4b** promotes Aβ$_{42}$ to adopt a structure with a relatively high β-sheet content.

Through the process of Aβ aggregation, its oligomeric species, which are produced via the pathway of fibrillation, are suspected to be toxic[4]. Therefore, we next examined the influence of glycopeptide **4b** on the oligomeric species formation of Aβ$_{42}$ with TEM imaging (Fig. 3c). When incubated alone for 2 days, Aβ$_{42}$ formed short worm-like protofilaments, which were recognized as intermediates through Aβ$_{42}$ aggregation[4]. In contrast, when Aβ$_{42}$ was incubated with **4b**, the amyloid

https://doi.org/10.1038/s41467-025-60978-w

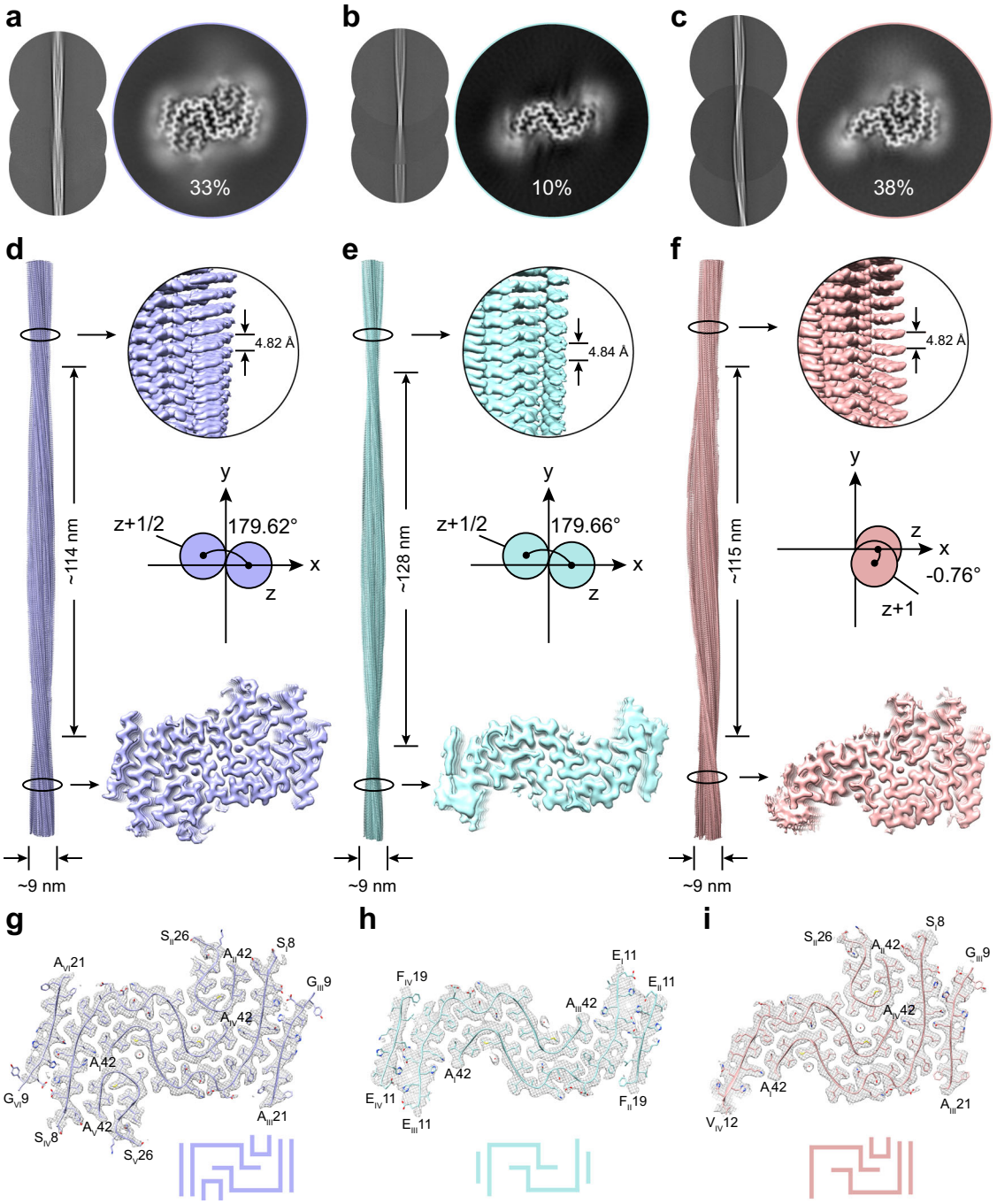

Fig. 4 | Cryo-EM structure determination of three major polymorphs of Aβ$_{42}$-4b fibrils. a–**c** 2D and 3D structural reconstructions with their proportions for Aβ$_{42}$-**4b**-P1 (left), P2 (middle) and P3 (right). **d**–**f** Density maps of Aβ$_{42}$-**4b**-P1, P2, and P3 with the fibril parameters marked, including the half pitch, fibril width, helical rise, and twist angle. **g**–**i** Cross-sectional views of the density map with the structure model built upon. The topology diagram is shown at the bottom of each structure.

peptide formed long and aggregated fibrils, whereas glycopeptide **4b** alone had no specific morphology. Further native PAGE results indicated that with increasing incubation time, coincubation with glycopeptide **4b** produced fewer oligomeric species of Aβ$_{42}$ within 48 h (Fig. 3d). Together, these results demonstrated that glycopeptide **4b** promoted Aβ$_{42}$ aggregation and decreased the proportion of oligomers.

Coassembly and cryo-EM structure determination of Aβ$_{42}$-glycopeptide 4b fibrils

To explore how glycopeptide **4b** promotes Aβ$_{42}$ fibrillation, we next examined whether glycopeptide **4b** and Aβ$_{42}$ coassemble in fibrils via stimulated emission depletion (STED) microscopy, which has been widely applied to observe nanoscale structures with subdiffractional resolution[35]. We synthesized FITC-labeled **4b** (**4b**-FITC) and Cy5-labeled Aβ$_{42}$ (Aβ$_{42}$-Cy5) and then incubated the mixture of the two samples for three days before imaging. As a control, these two labeled peptides were incubated separately under the same conditions and mixed immediately before imaging. The confocal images revealed high levels of colocalization for the co-incubated peptide sample, whereas no fluorescent signals of **4b**-FITC were observed in the control group (Supplementary Fig. 3a), presumably due to the inability of **4b** alone to assemble into observable nanostructures (Fig. 3c). This result suggests

https://doi.org/10.1038/s41467-025-60978-w

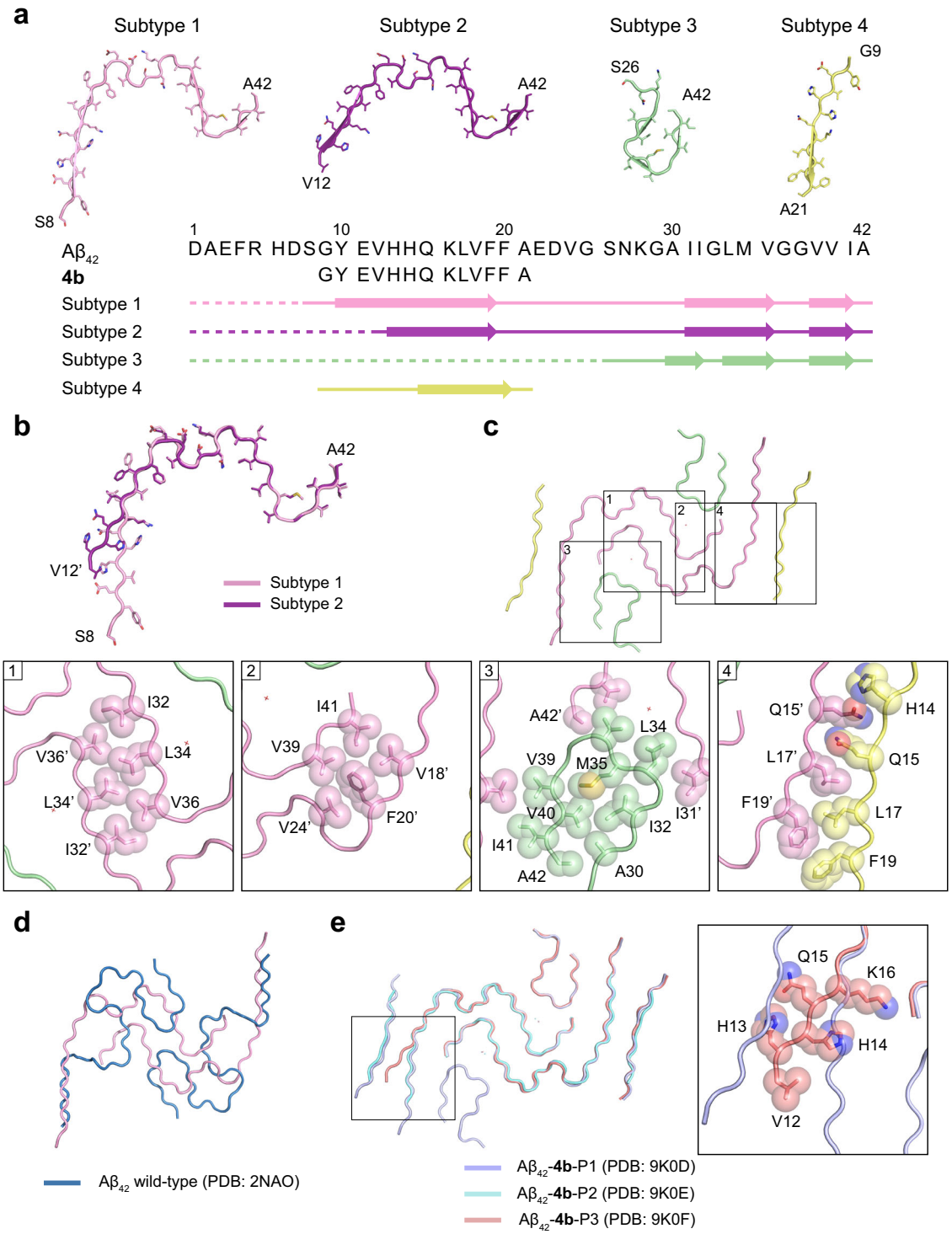

Fig. 5 | Structural analysis of three polymorphs of Aβ$_{42}$-4b fibrils. a Structures of the four subtypes (top) and the primary sequence with beta-strands formed in the fibril structures (bottom). **b** Structure overlay of subtype 1 and subtype 3. **c** One layer of Aβ$_{42}$-**4b**-P1 with subtype chains colored. The zoomed-in views of the side-chain interactions between different chains in Aβ$_{42}$-**4b**-P1 are shown at the bottom. **d** Structural comparison of two paired subtype 1 chains and Aβ$_{42}$ wild-type fibrils (PDB: 2NAO). **e** Structure overlay of Aβ$_{42}$-**4b**-P1, P2, and P3 with zoomed-in views of residues V12-K16.

the potential coassembly of Aβ$_{42}$ and **4b**. To further monitor the interplay between glycopeptide **4b** and Aβ$_{42}$ in the formed fibrils, we performed LC–MS analysis to quantify their stoichiometry. The results revealed a ratio of approximately 1:2 to 1:3 for Aβ$_{42}$/**4b** in the fibrils prepared from mixtures of the two peptides at ratios ranging from 1:1 to 1:4 (Supplementary Fig. 3b).

To further understand the structure of the fibrils coassembled by Aβ$_{42}$ and **4b** (termed Aβ$_{42}$-**4b** fibrils) at the atomic level, we determined the structure of the Aβ$_{42}$-**4b** fibrils via cryo-EM. Two-dimensional (2D) classification of the collected cryo-EM data revealed three major polymorphs of fibrils (Fig. 4a–c), which we termed Aβ$_{42}$-**4b** polymorph 1 (Aβ$_{42}$-**4b**-P1), Aβ$_{42}$-**4b** polymorph 2 (Aβ$_{42}$-**4b**-P2), and Aβ$_{42}$-**4b**

https://doi.org/10.1038/s41467-025-60978-w

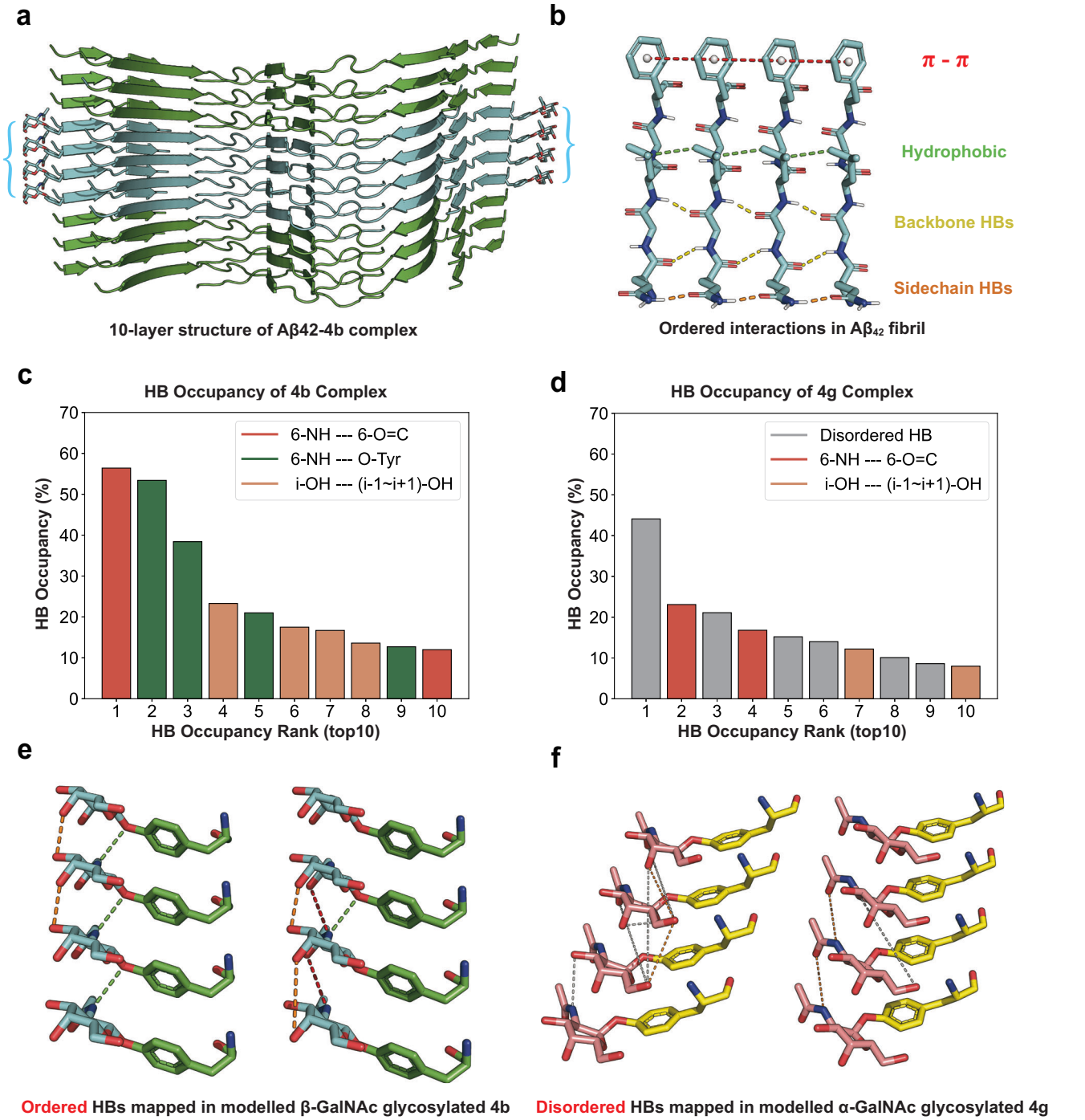

Fig. 6 | Rosetta modeling and MD simulations for Aβ$_{42}$-glycopeptide complexes. a An aerial view of an example structure of a 10-layer stacking model. O-linked tyrosines in the central 4 layers are shown as sticks. The central 4 layers colored in cyan for trajectory analysis are enclosed in brackets. **b** The ordered interlayer interactions observed in the fibrils. **c**, **d** Plots of the top 10 hydrogen bonds during the simulations ranked by occupancy. The red/green/orange-colored bars represent the HBs between the amide hydrogen and the carbonyl oxygen of the glycans, the HBs between the amide hydrogen and the phenol oxygen of Tyr, and the HBs between corresponding or adjacent hydroxyl groups in the glycans. The gray bars represent disordered HBs. **e**, **f** HBs mapped to the modeled structures of glycopeptides **4b** and **4g**. HBs are represented by colored dashed lines, and the meanings of the colors are the same as those of the bars. Source data are provided as a Source Data file.

polymorph 3 (Aβ$_{42}$-**4b**-P3). The proportions of Aβ$_{42}$-**4b**-P1, P2 and P3 were ~33%, 10% and 38%, respectively. Three-dimensional (3D) density maps were subsequently reconstructed for these polymorphs. On the basis of the gold-standard Fourier shell correlation (FSC) = 0.143 criterion, the overall resolutions of the density maps of Aβ$_{42}$-**4b**-P1, P2 and P3 were 2.6 Å, 2.8 Å and 2.8 Å, respectively (Supplementary Fig. 4). The Aβ$_{42}$-**4b**-P1 fibril features a half pitch of 114 nm (a pitch termed the length of a 360° helical turn of the entire fibril), a helical rise of 2.41 Å and a helical twist of 179.62° (Fig. 4d). Similarly, Aβ$_{42}$-**4b**-P2 displayed a half pitch of 128 nm, a helical rise of 2.42 Å, and a helical twist of 179.66° (Fig. 4e). However, Aβ$_{42}$-**4b**-P3 showed a distinct symmetry with the previous two polymorphs: C_1 in Aβ$_{42}$-**4b**-P3 and 2_1 in Aβ$_{42}$-**4b**-P1 and Aβ$_{42}$-**4b**-P2. The Aβ$_{42}$-**4b**-P3 fibril displayed a half pitch of 115 nm, a helical rise of 4.82 Å, and a helical twist of -0.76° (Fig. 4f).

Notably, the fibril cores of the three different fibril polymorphs consist of different numbers of polypeptide chains with distinct architectures within each layer (cross-section) perpendicular to the fibril axis. Specifically, $A\beta_{42}$-**4b**-P1 contains six individual polypeptide chains (Fig. 4g). However, both $A\beta_{42}$-**4b**-P2 and $A\beta_{42}$-**4b**-P3 contain four chains but with different spatial arrangements (Fig. 4h, i).

Structural analysis of three atomic structures of $A\beta_{42}$-4b fibrils

The high-quality density maps of the three $A\beta_{42}$-**4b** fibril polymorphs enabled us to unambiguously construct structural models of the three fibril polymorphs (Fig. 4g–i). Notably, four different structural conformations formed by various regions of $A\beta_{42}$ were identified in the three fibril polymorphs, which we termed subtypes 1-4 (Fig. 5a). The type 1 chain is composed of residues 8-42, which form three beta-strands and fold into a unreported W-shaped fold. The type 2 chain contains residues 12-42, which adopt an overall conformation similar to that of the subtype 1 chain. The major structural deviation between subtypes 1 and 2 lies in the N-terminal residue 12-16, which is important in holding the subtype 3 chain, as shown in in $A\beta_{42}$-**4b**-P1 (Fig. 5b). The type 3 chain consists of residues 26-42, which fold into a U-turn (Fig. 5a). The type 4 chain adopts a continuous beta-strand conformation. Strikingly, subtype 4 is composed of residues 9-21, which feature same sequence as that of **4b**. As we decreased the density contour, no additional density on the two ends of the subtype 4 chain was observed (Supplementary Fig. 5), suggesting that subtype 4 is formed by **4b** but not $A\beta_{42}$ molecules. In addition, we ruled out the possibility that the subtype 4 chain is derived from the same $A\beta_{42}$ molecule of the subtype 3 chain because of the extremely long distance between the subtype 4 chain and two different subtype 3 chains (Supplementary Fig. 6a). Notably, we only observed weak electron density of β-GalNAc on Tyr10 (Supplementary Fig. 6b, c), suggesting that β-GalNAc is not directly involved in fibril core formation and has high local flexibility, which is not visible via cryo-EM. Together, our cryo-EM structure strongly suggests that the density of subtype 4 is derived from **4b** but not from a fraction of the $A\beta_{42}$ molecule.

We next analyzed the structural arrangement of different chains in three fibril polymorphs of $A\beta_{42}$-**4b**-P1 fibrils. The $A\beta_{42}$-**4b**-P1 fibril core consists of six chains, including two copies of subtypes 1, 3 and 4 chains (Fig. 5c). Two subtype 1 chains pair together in the center of the fibril core via a steric zipper-like dry interface formed by the Ile32, Leu34 and Val36 residues (Fig. 5c). Moreover, Val39 and Ile41 of one chain also form hydrophobic interactions with Val18, Phe20 and Val24 from neighboring chains to maintain the fibril structure (Fig. 5c). Moreover, each subtype 3 chain is accommodated in the cavity formed by two subtype 1 chains via hydrophobic interactions (Fig. 5c). Strikingly, the subtype 4 chain, which adopts an elongated beta-strand, is attached on the surface of the fibril core and forms extensive and tight interactions with residues His13-Phe19 from the subtype 1 chain, including steric zippers formed by Gln15 and Gln15*, hydrophobic interactions formed by Leu17 and Leu17* and Phi-Phi stacking by Phe19 and Phe19* (Fig. 5c). Cryo-EM reconstruction of wild-type (WT) $A\beta_{42}$ under the same conditions revealed a fibril conformation (Supplementary Fig. 7) distinct from that of $A\beta_{42}$-**4b**, suggesting that **4b** interferes with the folding process, leading to the formation of entirely different fibril conformations. Compared with the structure of $A\beta_{42}$ WT determined by NMR[36–39] (Fig. 5d and Supplementary Fig. 8), the $A\beta_{42}$-**4b** complex packs more tightly with extensive hydrophobic interactions in the $A\beta_{42}$-**4b**-P1 fibril structure. Recent studies have shown time-dependent changes in fibril morphologies, as observed in S20G hIAPP[40,41], which are thought to arise from variations in stability and nucleation barriers among different fibril structures[42]. Therefore, the absence of previously reported WT $A\beta_{42}$ fibril morphologies in $A\beta_{42}$-**4b** fibrils is likely due to the strong stabilizing effect exerted by glycopeptide **4b** on the newly formed fibril structures.

$A\beta_{42}$-**4b**-P2 is formed by four chains, including two copies of subtypes 1 and 4 chains, which adopt conformations similar to those of $A\beta_{42}$-**4b**-P1 (Supplementary Fig. 9a). Notably, we observed fuzzy and weak densities, which are putative for subtype 3 chains in $A\beta_{42}$-**4b**-P2 (Supplementary Fig. 9b), suggesting that subtype 3 chains are highly flexible in $A\beta_{42}$-**4b**-P2. $A\beta_{42}$-**4b**-P3 contains four chains, including one copy of subtypes 1-4 (Fig. 5e). Subtypes 1 and 4 chains form nearly identical interfaces as those observed in P1 and P2 (Supplementary Fig. 9c). The N-terminal residue Val12-Lys16 of the subtype 2 chain flips apart from the fibril core, preventing the incorporation of both the subtype 3 and 4 chains into the fibril core, as observed in $A\beta_{42}$-**4b**-P1 and P2 (Fig. 5d). Notably, among all the measured $A\beta_{42}$-**4b** fibril structures, the stoichiometry of $A\beta_{42}$ and **4b** is ~2.4, which is consistent with the LC–MS data (Supplementary Fig. 3b). Taken together, the cryo-EM structures demonstrate that **4b** induces $A\beta_{42}$ to form three unique fibril structural polymorphs. In the $A\beta_{42}$-**4b** fibrils, **4b** adopts an elongated beta-strand and attaches to the outer surfaces of the fibrils by forming tight and extensive interactions with $A\beta_{42}$. These data clearly show a spatial arrangement with significant stabilization of the overall structure of the fibrils, which is in good accordance with the potent activity observed for **4b** in promoting $A\beta_{42}$ fibrillation (Fig. 3a). However, the distinct activity of **4b**, compared with that of non-glycosylated **4a** and other glycosylated forms, could not be explained at this stage.

MD simulations reveal that the glycan-based hydrogen-bond network formed by glycopeptides underlies a plausible aggregation-promoting mechanism

Given that additional density of glycosylation at Tyr10 was not observed via cryo-EM, we used computational methods to further explore the potential involvement of O-glycans in influencing fibril formation. Although computational tools have been established for O-glycosylation at Ser/Thr[43–45], methods for modeling Tyr-O-glycosylation on peptides have yet to be developed. Therefore, we first developed a RosettaScripts[46] protocol for glycosylation with various monosaccharides linked to Tyr (see *Modeling Tyr-O-glycosylation in Rosetta* in Methods for details), addressing the issue of not observing glycosylation density in Cryo-EM structures. Considering that the excessive length of the original fibril (~120 nm) could result in an overly heavy computational load for MD simulations, we instead used PyMOL to build a 10-layer stacking structure of the isolated $A\beta_{42}$ fibril, as well as various $A\beta_{42}$-glycopeptide complexes (Fig. 6a). We subsequently performed MD simulations for these 10-layer fibril structures using Amberff14SB force field[47], and the parameters related to Tyr-O-glycosylation were obtained from GLYCAM06[45] and GAFF[48] (see *MD simulation settings* in Methods for details). To eliminate the influence of boundary layers, we extracted the central 4 layers (layers 4 to 7) from the 10-layer model for trajectory analysis (Fig. 6a, enclosed in brackets), as these layers may better reconstruct the authentic context in fibrils.

By examining the isolated $A\beta_{42}$ fibril model, we found that the core hydrophobic region was stable during the simulation (Supplementary Fig. 10a). However, in the absence of the interacting glycopeptides, the flanking N-termini of $A\beta_{42}$ tended to swing in the aqueous solution with higher RMSF (root mean squared fluctuation, Supplementary Fig. 10b, c), which is consistent with the observation from cryo-EM structures that the $A\beta_{42}$-**4b** complex packs more tightly than $A\beta_{42}$ WT does. These observations further support that the glycopeptides likely provide a squeezing force to the $A\beta_{42}$ fibril through interactions with the $A\beta_{42}$ N-termini, leading to more tightly packed fibril structures with strengthened internal hydrophobic contacts. To delve deeper into the origin of such impacts of glycopeptides, we considered that an important factor promoting fibril formation is ordered interlayer interactions. Here, "ordered" refers to those interactions between two layers that have similar patterns, such as the

https://doi.org/10.1038/s41467-025-60978-w

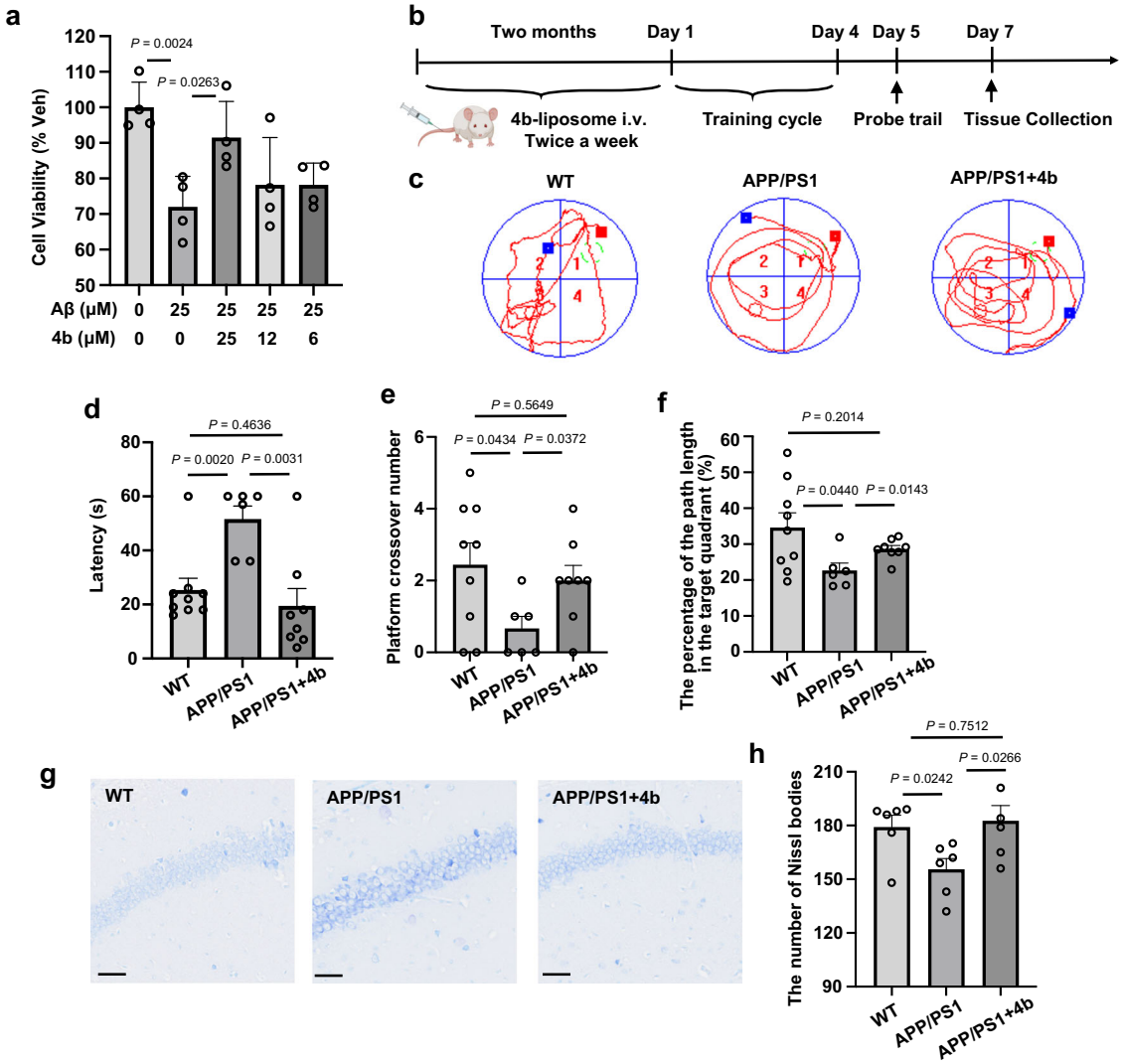

Fig. 7 | β-GalNAc $Aβ_{9-21}$ (4b) rescues the cell toxicity of $Aβ_{42}$, cognitive impairment, and neuron loss in APP mice. a Cell viability assay performed with the CCK-8 method ($n = 4$). SH-SY5Y cells were incubated with different concentrations of Aβ and **4b** for 24 h. The viability of untreated cells was set as 100%. **b** Schematic drawing of the schedule of the Morris water maze (MWM) test and tissue collection in C57BL/6 J mice treated with liposome vehicle (WT, wild-type, $n = 9$), APP/PS1 mice liposome vehicle (APP/PS1, $n = 6$), and APP/PS1 mice treated with **4b**-liposomes (APP/PS1 + **4b**, $n = 8$). i.v., intravenous injection. Created in BioRender. Yang, X. (2025) https://BioRender.com/55v38fv. **c** Representative swimming traces obtained during the probe trial. Red square, the starting point. The blue square represents the end point. Red circle, hidden platform. **d** Escape latency during the probe trial. **e** The number of times the mice passed through the area of the hidden platform during the probe trial. **f** The percentage of path length in the target quadrant of the hidden platform during the probe trial. **g** Nissl staining of the hippocampal region of the mice. Scale bar, 50 μm. **h** The number of neurons in the hippocampal region of the mice in (**g**) ($n = 6$). Statistical significance was assessed using two-side Student's *t*-test. All values are presented as the means ± s.e.m.s. Source data are provided as a Source Data file.

ordered backbone hydrogen bonds (HBs), side-chain HBs, hydrophobic stacking, and π-π interactions observed in $Aβ_{42}$ fibrils (Fig. 6b). Therefore, we aimed to study possible glycan–glycan interactions, particularly interlayer HBs, considering the relatively flexible and dynamic nature of the glycans that are not observed in the cryo-EM structures but may contribute to stabilizing the supramolecular assembly. We analyzed the HB networks associated with the glycans of the modeled fibrils by plotting heatmaps for each HB during the simulations (Supplementary Fig. 11) and examined the top 10 HBs in the modeled structures ranked by occupancy. The occupancy of an HB can be regarded as a measurement of contribution to stability and is defined as the proportion of frames in the extracted trajectory where the HB being analyzed is in a formed state. A representative analysis of β-GalNAcylated glycopeptide **4b** and α-GalNAcylated glycopeptide **4 g** is shown in Fig. 6c, d, as the two glycans differ only in their anomeric stereochemistry. The HBs were then mapped in the initial modeled structure for clarity (Fig. 6e, f), and the representative conformations during the simulations are shown in Supplementary Fig. 12. The results indicated that two types of HBs were predominant, with the highest occupancy in the trajectory of **4b**. One is the HB between the amide hydrogen of GalNAc and the amide oxygen of GalNAc or the phenol oxygen of Tyr in the neighboring layer, and the other is the HB between the axial 4-OH of GalNAc and the 3-OH of GalNAc in the neighboring layer. These interactions between the corresponding or adjacent groups in neighboring layers match the "ordered" interlayer interactions observed in the Aβ fibrils (Fig. 6b). In contrast to the case of **4b**, in the modeled fibril with **4g** containing α-GalNAc, the predominant HBs with the highest occupancy were formed between the 3-OH and the amide carbonyl oxygen. These two groups are located on opposite sides of the glycan ring, leading to a formed HB requiring misaligned glycans and necessitating significant conformational changes that contribute less to stability (Supplementary Fig. 12). Although several

ordered HBs between the amide NH and the carbonyl oxygen were observed in the α-GalNAc of glycopeptide **4g**, their occupancy was relatively low. Notably, all these HBs do not have particularly high occupancy, indicating that the conformation of the glycans is indeed quite dynamic, which is also consistent with their absence in the cryo-EM structures. Taken together, the unique axial 4-OH of GalNAc and the equatorial β-conformation of the glycosylation facilitate the formation of a relatively ordered HB network between glycans, which may explain the superior effect of **4b** in promoting aggregation. Overall, MD simulations suggested that properly structured glycans on short peptides may form well-arranged HB networks, providing stabilizing forces for fibril formation and ultimately promoting the aggregation of $A\beta_{42}$. This glycan-enabled interlayer "ligand–ligand" interaction represents a distinctive type of stabilizing mode in aggregation models beyond the reported modes, such as π–π stacking[49].

β-GalNAc $A\beta_{9\text{-}21}$ rescues the cell toxicity of $A\beta_{42}$, cognitive impairment and neuron loss in APP mice

A potential application of aggregation-promoting glycopeptide **4b** is to alleviate the toxicity of $A\beta_{42}$ through decreasing the amount of protofibers and oligomers, which are widely regarded as the toxic species of β-amyloid peptide[50,51]. To test this hypothesis, we treated neuroblastoma SH-SY5Y cells and rat primary neurons with $A\beta_{42}$ and **4b**. As shown in Fig. 7a and Supplementary Fig. 13a, treatment with $A\beta_{42}$ alone caused cell death. However, with the addition of **4b**, the cell toxicity induced by $A\beta_{42}$ decreased in a dose-dependent manner. Moreover, **4b** alone showed no cytotoxicity (Supplementary Fig. 13b). To further validate the ability of **4b** to rescue $A\beta_{42}$ toxicity, we carried out experiments on APP/PS1 transgenic mice, which were intravenously injected with **4b** encapsulated in liposomes twice a week. Notably, via this liposome-assisted strategy, glycopeptides can be delivered across the blood–brain barrier (BBB) into the brain with acceptable efficiency (Supplementary Fig. 14)[52]. In the control groups, APP mice and wild-type mice were also injected with liposome-containing vehicle. After 2 months of treatment, the Morris water maze (MWM) test was conducted to investigate the spatial cognitive performance of the mice (Fig. 7b). As shown in Fig. 7c, the AD mice treated with glycopeptide **4b** presented more spatially oriented swimming behavior than did the AD mice in the control group. Furthermore, compared with untreated AD mice, AD mice treated with **4b** presented significantly shorter latencies to find the hidden platform, more platform crossovers, and a greater percentage of path length in the target quadrant (Fig. 7d–f). Notably, the behavior of the **4b**-treated mice was similar to that of the wild-type mice, suggesting that **4b** could effectively alleviate cognitive impairment. Moreover, to further assess neuronal damage in the hippocampus, we utilized Nissl staining to evaluate neuronal activity in the mouse brain[53,54]. Nissl staining, which reflects the distribution and morphology of Nissl bodies, revealed that the AD mice treated with **4b** exhibited a greater density of Nissl-positive neurons compared to the untreated group (Fig. 7g, h). Additionally, no obvious in vivo systemic toxicity of **4b** was observed in the histopathology assays (Supplementary Fig. 13c). Together, these results demonstrated that glycopeptide **4b** may rescue Aβ-induced neurotoxicity in the brains of APP mice.

Discussion

Here, we designed a series of Tyr O-glycosylated $A\beta_{9\text{-}21}$ peptides to explore the regulatory effects of their different glycans and the stereochemistry of their glycosidic bonds on $A\beta_{42}$ aggregation. After ThT and BLI screening, we found that β-GalNAc-modified $A\beta_{9\text{-}21}$ had the strongest effect on promoting $A\beta_{42}$ aggregation among all the glycopeptides. Moreover, we confirmed that β-GalNAc $A\beta_{9\text{-}21}$ enables $A\beta_{42}$ to form aggregates with a higher β-sheet content than $A\beta_{42}$ alone, which decreases the amount of $A\beta_{42}$ oligomeric species. Mechanistic studies demonstrated that β-GalNAc $A\beta_{9\text{-}21}$ could bind with $A\beta_{42}$ and coassemble together for fibrillation. On the basis of the high-resolution cryo-EM structures of $A\beta_{42}$-**4b** fibrils, we discovered that **4b** may adopt a β-conformation and form extensive interactions with $A\beta_{42}$ to induce $A\beta_{42}$ to form a series of distinct fibril structures. The molecular dynamics simulations emphasized the importance of structured hydrogen bond networks, primarily due to the properly positioned amide NH and axial 4-OH in β-GalNAc, illustrating the rationale of glycopeptide **4b**-promoted $A\beta_{42}$ aggregation. Based on these results, we further evaluated the effects of the glycopeptide on $A\beta_{42}$ neurotoxicity. In vitro and in vivo assays revealed that treatment with β-GalNAc $A\beta_{9\text{-}21}$ reversed the toxicity of $A\beta_{42}$ in SH-SY5Y cells and alleviated spatial cognitive deficits in APP/PS1 mice. Together, the findings of this study demonstrated the potential of applying glycopeptides to modulate amyloid protein aggregation.

The sequences of aggregation-prone proteins have been exploited to discover aggregation modulators. However, owing to the self-recognizing features of these proteins, the identified peptide fragment can occupy the requisite regions for aggregation and therefore is mostly inhibitors[55,56]. While a wide range of examples support that protein glycosylation generally impedes protein–protein interactions[57,58] and inhibits aggregation[25,59], we demonstrated in this work that glycans could act as effective modifications of Aβ-interacting peptides to generate an $A\beta_{42}$ aggregation enhancer, which expands the chemical toolbox of modulators for amyloid protein aggregation beyond traditional small molecules and peptides[18,60]. Since the aggregation of fibrillation-prone proteins is strongly associated with the development of neurodegenerative diseases, developing regulators that interfere with the pathological aggregation process is highly valuable. Efforts have been made to discover molecules with inhibitory effects on amyloid protein aggregation over the past few decades[14]. As oligomers, instead of mature fibrils, have been proposed as toxic species in the disease process, aggregation promotors may be potentially applicable for alleviating toxicity[51]. Notably, although we have shown that **4b** can alleviate AD symptoms in mice, the detailed mechanism remains to be fully elucidated. Future studies should explore the potential involvement of carbohydrate-binding proteins in Aβ clearance, where the glycopeptides discovered in this work could serve as essential molecular probes.

Glycopeptides represent a unique class of modulators that target Aβ aggregation through mechanisms distinct from those of small molecules and antibodies. While small molecules typically bind to the hydrophobic regions of Aβ to disrupt fibril formation[61], and antibodies recognize specific epitopes to neutralize toxic oligomers[62], glycopeptides leverage their distinctive structural features to modulate aggregation kinetics and potentially redirect the aggregation pathway. Compared with other Aβ aggregation modulators, glycopeptides offer advantages derived from both their peptide and glycan components. The peptide structure allows for ease of preparation, structural modification for enhanced efficacy and specificity, and the ability to interfere with large protein-protein interaction surfaces[63]. Additionally, the glycan moiety in glycopeptide may improve pharmacokinetic properties, enhance biocompatibility, and potentially introduce carbohydrate-related signaling pathways for further modulation. However, challenges remain in using glycopeptides to target aggregation-prone proteins, including issues with inefficient brain delivery and potential off-target effects in vivo caused by the glycan structure. Addressing these limitations will be crucial for advancing glycopeptide-based strategies for the treatment of amyloid-related diseases.

Currently, mechanistic insight into how aggregation regulators interact with amyloid proteins remains extremely limited[16], particularly given the lack of direct evidence that can provide a structural basis. By means of cryo-EM, we are able to characterize the structure of coassembled fibrils formed by glycopeptide **4b** and $A\beta_{42}$ and illustrate significant and

unprecedented structural changes in the $A\beta_{42}$ fibril polymorphism induced by the glycopeptide at the atomic level. The molecular dynamics simulations in this study not only shed light on the critical role of specific glycans in the accelerated fibril formation process but also establish a protocol for modeling O-glycosylation on tyrosines in Rosetta and Gromacs, which are rare posttranslational modifications across various species but have attracted increasing attention[64,65]. Notably, to the best of our knowledge, this is the first report on the modeling and simulation of tyrosine glycosylation in Rosetta and Gromacs. The force field parameters we used to model tyrosine glycosides are inherited from classical glyco-modification systems and have not been optimized specifically. There is still much work to be done in developing computational tools for such a rare modification. Nevertheless, our work provides an example demonstrating that computational tools can be used to study these highly flexible and dynamic glycosylated molecules. Overall, on the basis of the glycopeptide structures we discovered, we anticipate that such a combination of glycans and peptides may become a new modality for developing modulators of aggregation-prone proteins.

Methods

Ethical statement

Male C57BL/6 mice and APP/PS1 transgenic mice on a C57BL/6 background were supplied by Beijing Vital River Laboratory Animal Technology Co., Ltd Experiments were approved by the Institutional Animal Care and Use Committee of Peking University (LA2021221). All mice were housed in an SPF animal facility (light/dark cycle: 12 h/12 h, temperature: 20–26 °C, humidity: 40–70%) with ad libitum access to food and water. After the end of the experiment, the mice were immediately euthanized.

Materials

All commercial materials (Aldrich, GL Biochem, TCI, Acros, J&K, etc.) were used without further purification. All solvents were reagent grade or HPLC grade (Fisher, Sigma, Across, Oceanpak). Filtration of the crude peptide was performed via a Bulk GHP Acrodisc 13 mm syringe filter with a 0.22 µm GHP membrane. Yields refer to chromatographically and spectroscopically pure materials unless otherwise stated.

Syntheses of the glycosylated amino acid building blocks[28]

Full synthetic procedures can be found in Supplementary Information.

Assembly of $A\beta_{9\text{-}21}$ peptides on Rink amide resin

Peptides were synthesized using a CEM automated peptide synthesizer following standard Fmoc-based SPPS protocols with DMF as the solvent. Fmoc deprotection was performed twice for 3 min each using 20% piperidine in DMF (v/v) at 70 °C. Amino acid coupling was carried out for 3 min at 70 °C using a fourfold excess of Fmoc-protected amino acids, HATU/HOBt (1:1, 4 equiv), and DIEA (4 equiv). For amino acids following sterically hindered residues (e.g., His and Val), the coupling cycle was repeated to ensure completion. The following αN-Fmoc-protected amino acids (purchased from Novabiochem, GL Biochem, or CS Bio) were employed in SPPS: Fmoc-Ala-OH, Fmoc-Asn(Trt)-OH, Fmoc-Asp(OtBu)-OH, Fmoc-Glu(OtBu)-OH, Fmoc-Gln(Trt)-OH, Fmoc-Gly-OH, Fmoc-His(Trt)-OH, Fmoc-Leu-OH, Fmoc-Lys(Boc)-OH, Fmoc-Phe-OH, Fmoc-Tyr(tBu)-OH, Fmoc-Val-OH.

For glycopeptides, glycosylated amino acid building blocks (1.2 equiv, coupled twice) were manually incorporated onto the peptidyl resin. Each coupling was performed for 2 h at room temperature in 2 mL DMF using HATU (1.2 equiv) and DIEA (2.4 equiv), with continuous shaking. After successful incorporation of the glycosylated residues, the peptidyl resin was returned to the CEM synthesizer for automated coupling of the remaining amino acids.

Cleavage of the peptidyl resin and deprotection of the (glycosylated) $A\beta_{9\text{-}21}$

Resin cleavage and global deprotection were performed in a cocktail solution of TFA/H_2O/TIPS (95:2.5:2.5, v/v/v) for 2 h. The resin was then removed by filtration, and the filtrate was concentrated under a nitrogen atmosphere. The resulting residue was washed with cold diethyl ether to give a white solid. The crude (glyco)peptide was treated with 1 M NaOH at the concentration of 2 mg/ml for 1 h to remove the acetyl group in the building blocks from the peptide. The reaction was then quenched by addition of neat TFA, and the mixture was lyophilized, followed by dissolving in a mixture of acetonitrile and water. The resulting solution was ready for HPLC purification after filtration.

$A\beta_{42}$ preparation and pretreatment

$A\beta_{42}$ and biotin or azide-labeled $A\beta_{42}$ were synthesized through solid-phase peptide synthesis according to previously reported protocol[25]. Briefly, H-Rink amide ChemMatrix resin (0.05 mmol, loading = 0.45 g/mmol) was pre-swollen in DMF (5 mL) for 10 min. A mixture of Fmoc-Lys (Boc)-OH (117.1 mg, 0.25 mmol), HATU (95 mg, 0.25 mmol), and DIEA (84 µL, 0.5 mmol) in DMF (2 mL) was added. The reaction mixture was then agitated at room temperature for 30 min, and then filtered. The coupling protocol was repeated for twice. Then, a solution of 20% piperidine in DMF (v/v, 3 mL) was added, and the mixture agitated at room temperature for 2 × 5 min, after which the resin bed was filtered and washed with DMF (3 × 3 mL). This protocol was repeated a further 5 times, such that six lysine residues were coupled to the resin in total. A solution of HMBA (46 mg, 0.3 mmol), HOBt (40 mg, 0.3 mmol), and DIC (46.5 µL, 0.3 mmol) in DMF (2 mL) was then added onto the resin to introduce the HMBA linker. Then, automated peptide synthesis was performed on a CEM peptide synthesizer. Peptides were synthesized following the protocol using DMF as solvent, deblock for 5 min (×2) in piperidine/DMF (20/80, v/v) at 50 °C, couple for 10 min using excess amino acids (10 equiv) and HATU/HOBt (1:1, 10 equiv) as coupling reagents at 50 °C. The coupling cycle was repeated as needed for amino acids after steric hindered residues such as Arg, Ile, His, and Val. The following αN-Fmoc-protected amino acids from Novabiochem, GL Biochem or CS Bio were employed in SPPS: Fmoc-Ala-OH, Fmoc-Arg(Pbf)-OH, Fmoc-Asn(Trt)-OH, Fmoc-Asp(OtBu)-OH, Fmoc-Glu(OtBu)OH, Fmoc-Gln(Trt)-OH, Fmoc-Gly-OH, Fmoc-His(Trt)-OH, Fmoc-Ile-OH, FmocLeu-OH, Fmoc-Lys(Boc)-OH, Fmoc-Phe-OH, Fmoc-Ser(tBu)-OH, Fmoc-Tyr(tBu)OH, Fmoc-Val-OH. Biotin (10 equiv) or Fmoc-azidolysine (10 equiv), HATU (10 equiv), and DIEA (20eq) were added to the resin and couple for 2 h, follow by Fmoc removal and washing. $A\beta_{42}$ and biotin-labeled $A\beta_{42}$ were treated with 10% v/v NH_4OH (1 mg/mL) to remove preformed aggregates. Following reconstitution, the peptide was left at room temperature for 10 min and sonicated for 5 min at a frequency band of 50–60 Hz. Sonicated samples were then centrifuged at 16,000 × g for 10 min at room temperature. The supernatant was dispensed as 200 µL aliquots (0.20 mg), which were lyophilized and stored at −80 °C. To avoid the aggregation process during the storage, all samples were retreated with 10% w/v NH_4OH (1 mg/mL) before further experiments.

HPLC analysis and purification

All HPLC separations involved a mobile phase of 0.05% (v/v) TFA in water (solvent A) and 0.04% (v/v) TFA in acetonitrile (solvent B). Analytical LC–MS analyses were performed via a Water Alliance e2695 Separations Module equipped with an Agilent C18 column (5.0 µm, 4.6 × 150 mm, 0.4 mL/min), a Water 2489 UV/Visible (UV/Vis) Detector, and a Waters SQD mass spectrometer (Alliance e2695-SQD). The wavelengths of the UV detector were set to 210 nm and 220 nm. Analytical HPLC separations were performed via an Agilent

Technologies 1260 Infinity LC system. Preparative HPLC separations were performed via two Shimadzu LC-20AR semipreparative solvent delivery units, a Shimadzu SPD-20A UV detector, and a Shimadzu CBM-20A system controller equipped with a Dr. Maisch ReproSil 300 C18 column (5.0 μm, 20 × 250 mm) at a flow rate of 12 mL/min. The wavelengths of the UV detector were set to 210 and 220 nm.

Thioflavin T (ThT) assay

A solution of 1 mM thioflavin T (ThT) was freshly prepared prior to every experiment. This stock solution was then diluted in ice-cold 10 mM PBS (pH 7.4) to a final concentration of 10 μM. $Aβ_{42}$ (6 μM) and different glycopeptides (12 μM) were reconstituted in ice-cold 10 μM ThT in 10 mM PBS (pH 7.4) and immediately transferred to an opaque black 96-well plate on ice in triplicate. Specifically, for the dose-dependence assay of **4b**, $Aβ_{42}$ (8 μM) or $Aβ_{40}$ (HARVEYBIO, cat. DR0607, 8 μM) and different ratios of glycopeptides were reconstituted according to the indicated conditions. The plate was then sealed with a clear plastic cover and placed in a plate reader (BioTek Synergy Neo 2) at 37 °C, with the plate vibrating every 10 min. The fluorescence intensity was monitored at 440 nm (excitation) and 485 nm (emission) for 600 min with 30-min intervals between each read. The ThT signal of the peptides was subtracted from the background signal (10 μM ThT in 10 mM sodium phosphate buffer (pH 7.4) with no peptide). Kinetic parameters (Ymax, rate constant Kagg and half-life t1/2) were calculated as described[66].

Circular dichroism (CD) spectroscopy

Lyophilized $Aβ_{42}$ and glycopeptides were dissolved in PBS buffer (pH 7.4) and then incubated at 37 °C for 24 h. The secondary structure of the peptide was quantified with a circular dichroism spectrophotometer (BioLogic MOS-450) at room temperature with a bandwidth of 1 nm and a read time of 200 nm/min from 230 to 190 nm. To determine the coassembly secondary structure, $Aβ_{42}$ and **4b** were incubated at the indicated ratios at 37 °C for 24 h and then measured. Mdeg values were subtracted from the baseline values (10 mM sodium phosphate buffer (pH 7.4) with no peptide). The calculations were conducted via the BeStSel method[67].

Transmission electron microscopy (TEM) imaging

Lyophilized $Aβ_{42}$ was dissolved with or without **4b** in PBS buffer at a concentration of 50 μM, and the solution was incubated at 37 °C for 2 days. Then, 5 μL of incubated peptide solution was loaded onto the copper grids of carbon support films (200 mesh) for 1 min. Excess solution was removed by blotting with filter paper, followed by the addition of 5 μL of negative stain reagent (2% aqueous phosphotungstic acid) and staining for 1 min. After removing the remaining liquid with filter paper, the copper grids were allowed to dry in air overnight. Copper grids were then directly imaged via a transmission electron microscope (JEM-1400 PLUS).

Native PAGE

$Aβ_{42}$ was dissolved with or without **4b** in PBS buffer at a concentration of 50 μM, followed by incubation at room temperature for different durations. At each time point during the real-time assay, a 15 μL aliquot was taken and immediately flash frozen in liquid nitrogen. The aliquot was mixed with Native-PAGE loading buffer (Biosharp; BL529A) and loaded onto an Invitrogen 4%–20% precast gel (Invitrogen; XP04200PK). The gel was run in Tris-glycine buffer at 150 V for 25 min and 225 V for 35 min and then stained via a standard silver staining protocol.

Binding affinity evaluation with biolayer interferometry (BLI)

Biotinylated $Aβ_{42}$ was dissolved in working buffer (PBS buffer with 0.02% Tween and 5% DMSO) at a concentration of 20 μg/ml and immobilized onto streptavidin biosensors. Biolayer interferometry (BLI) assays were performed in 96-well plates on an Octet R8 (Sartorius) Protein Analysis System. The wells were filled with 200 μL of working buffer or peptide solution (prepared in working buffer). Biotinylated peptide was immobilized onto the streptavidin tip for 300 s. Sensors were then dipped into a working buffer for 60 s, a glycopeptide solution (1.25 μM, 2.5 μM, 5 μM, 10 μM, or 20 μM) for 150 s, and finally into kinetic buffer for 200 s. Measurements were carried out at 30 °C.

Imaging of coassembled fibrils via STED microscopy

N_3-$Aβ_{42}$ was dissolved in DPBS at 100 μM and added to DBCO-Cy5 (100 μM) to perform the click reaction. After incubation at 37 °C in the dark for 10 min, the mixture was lyophilized until use. Cy5-$Aβ_{42}$ and FITC-**4b** were dissolved in PBS buffer according to the conditions for different samples: Cy5-$Aβ_{42}$ (100 μM), FITC-**4b** (100 μM), and Cy5-$Aβ_{42}$ + FITC-**4b** (100 μM + 100 μM). The samples were incubated at 37 °C for three days, followed by centrifugation to remove the supernatant and collect the resulting fibrils. Then, Cy5-$Aβ_{42}$ + FITC-**4b** was reconstituted to a final concentration of 100 μM, while the resulting precipitates of the Cy5-$Aβ_{42}$ and FITC-**4b** samples were mixed to a final concentration of 100 μM each. Both premixed $Aβ_{42}$ + FITC-**4b** and postmixed $Aβ_{42}$ + FITC-**4b** samples were imaged via STED microscopy (Abberior) to visualize the resulting fibrils.

UPLC–MS quantification

$Aβ_{42}$ and **4b** were dissolved in 10% $NH_3·H_2O$ separately at concentrations of 125, 500, 750, 1000, 1250, and 1500 ng/mL and subjected to UPLC-MS (Waters ACQUITY UPLC I-Class and Waters Xevo TQ-S). The standard curve was then drawn with the mass peak area to determine the concentration. For the fibril coassembly assay, $Aβ_{42}$ was mixed with **4b** at different molar ratios (final concentration, Aβ: 5 μM; **4b**: 5, 10, 15, and 20 μM) in phosphate buffer (50 mM, pH 7.4) for 3 replicates. After 3 days of incubation at 37 °C, the mixtures were centrifuged at 13,000 × *g* for 10 min. The resulting pellets were dissolved in 300 μL of $NH_3·H_2O$ (10%), sonicated for 10 min, and diluted 10-fold before being subjected to UPLC–MS (3 injections per sample). The fibril ratio was calculated through each peptide's mass peak area and standard curve.

Cryo-EM sample preparation and data collection

$Aβ_{42}$ (50 μM) and **4b** (50 μM) in 50 mM phosphate buffer (pH 7.4) were incubated at 37 °C for 24 h at 220 rpm. Samples containing $Aβ_{42}$ and **4b** were applied to glow-discharged holey carbon copper grids (Quantifoil, 300 mesh, R2/1) and then plunged frozen in liquid ethane after blotting with filter paper by using Vitrobot Mark IV (Thermo Fisher). The cryo-EM micrographs were collected on a Titan Krios G4 transmission electron microscope (Thermo Fisher), which was operated at 300 kV with a BioContinuum K3 direct detector (Gatan), using a GIF Quantum energy filter (Gatan) with a slit width of 20 e^-V to remove inelastically scattered electrons. Forty frames per micrograph were recorded in super-resolution mode with a pixel size of 0.83 Å $pixel^{-1}$ at ×105,000 magnification. The total dose was ~55 $e^-/Å^2$ with an exposure time of 2 s, and automated cryo-EM data collection was performed via EPU software (Thermo Fisher), with defocus values ranging from −1.0 to −2.0 μm.

Imaging preprocessing

The collected cryo-EM data were corrected for beam-induced motion of movie frames with alignment and dose weighting via MotionCorr2[68]. Then, CTFFIND-4.1.8[69] was applied to estimate the contrast transfer function of motion-corrected images. After that, the following helical reconstruction was performed in RELION version 3.1[70–72].

Helical reconstruction

A total of 154,300 picked fibrils from 4556 preprocessed micrographs were extracted to segments in the box size of 720 pixels with an

interbox distance of 59.8 Å. Next, several iterations of reference-free two-dimensional (2D) classification were performed to calculate the helical parameters, and the segments contributing suboptimal 2D class averages with a decreasing in-plane angular sampling rate from 12° to 0.5° and the $T = 2$ regularization parameter were discarded. For the three polymorphs of fibrils separated after 2D classification, the selected particles were used to generate an initial 3D reference de novo via the *relion_helix_inimodel2d* program for the following 3D classification ($K = 3$) with a 60 Å low-pass filter. A local search of symmetry to optimize the helical twist and rise was carried out after the separation of β-strands was shown to select the clearest classes. Then, 3D optimization of the helical parameters was carried out. Finally, the overall resolutions of the 3 classes of $A\beta_{42}$-**4b** fibrils were reported as 2.6 Å, 2.8 Å, and 2.8 Å, respectively, according to the gold-standard FSC = 0.143 criterion.

Atomic model building and refinement

On the basis of density maps after postprocessing, the atomic models of 3 classes of fibrils were built de novo and improved in COOT[73]. Three-layer models were subsequently generated in Chimera and refined via the real-space refinement program in PHENIX[74,75]. Additional details are shown in Supplementary Table 2.

Cell line treatment and cytotoxicity evaluation

Human neuroblastoma SH-SY5Y cells were purchased from iCell (Cat#iCell-h187) and cultured in Dulbecco's modified Eagle's medium (M&C; CM10013) supplemented with 10% fetal bovine serum (FBS) and 0.1 mg/mL penicillin/streptomycin (M&C; CC004) at 37 °C in humidified 5% CO_2 air. SH-SY5Y cells (5,000 cells/well) were plated onto 96-well plates. To evaluate the influence of **4b** on the cytotoxicity of $A\beta_{42}$, $A\beta_{42}$ (25 μM in DMEM) was incubated with different concentrations of **4b** in cells for 24 h, with 4 replicates per group. To evaluate the toxicity of **4b**, different concentrations of **4b** were dissolved in DMEM and used to treat SH-SY5Y cells for 24 h. The cytotoxicity was evaluated with a Cell Counting Kit-8 (Bioss, BA00208) according to the standard protocol after incubation.

Cell viability of primary neuron

Rat primary cortical neuron cultures were isolated from neonatal mice within 24 h of birth[76]. Cells were cultured in NBPG medium (Neurobasal medium (Gibco), B-27 supplement (Gibco), Penicillin/Streptomycin, and GlutaMAX (Gibco)) in Poly-D-Lysine (BBI)-coated 96-well plate at a density of 80,000 cells per well, with the addition of cytarabine (5 μM), in a humidified 5% CO_2 incubator. Half of the media was replaced every 2 days. Glycopeptide **4b** and HFIP-treated $A\beta_{42}$ were dissolved in NBPG medium and incubated at 37 °C for 24 h. The resulting solutions were then diluted to the appropriate concentrations and added to neuron cultures at day 5 in vitro. After 48 h of treatment, cell viability was accessed using CellTiter-Glo® Luminescent Cell Viability Assay Kit (Promega).

Preparation of liposomes and evaluation of brain delivery ability

The **4b**-containing liposome was prepared according to a previously reported method[52]. Briefly, lipid mixtures (11.79 mg DOPC, 3.36 mg cholesterol, and 3.48 mg DSPE-PEG2000) were dissolved in 2 mL chloroform, dried into a lipid film, and kept in vacuo overnight. The dried lipid film was rehydrated in the presence of PYREXTM glass beads in the dark with 1 mL of water or a 1 mL aqueous solution of **4b**- or Cy5-labeled **4b** (200 μg). The resulting mixture was ultrasonicated for 15 min, followed by 10 freeze–thaw cycles of quenching in liquid N_2 and then immersion in a 37 °C water bath. The suspension was then extruded with a miniextruder (Avanti Polar Lipids, Inc.) at r.t. using a polycarbonate membrane with a pore size of 200 nm. After 20 cycles of extrusion, the liposomes were purified by gel filtration through a Sephadex G-50 mini-column. The purified liposomes were stored at 4 °C. The percentage of **4b** encapsulated in liposomes was quantified via HPLC according to the concentration–UV response standard curve of **4b**. To verify the BBB penetration ability of liposome-encapsulated **4b**, 5 μl of liposome-encapsulated **4b**-Cy5 or **4b**-Cy5 or vehicle was intravenously injected through the tail vein, followed by quantification of the fluorescent signal after 4 h with an IVIS SPECTRUM (Perkin Elmer).

Water maze experiment

Male C57BL/6 wild-type and APP/PS1 transgenic mice aged 9–10 weeks were used. APP/PS1 mice were randomly assigned to receive either 5 μL PBS or 5 μL liposome-encapsulated compound **4b** via intraperitoneal injection, twice weekly for two months. Wild-type mice received 5 μL PBS under the same regimen. Following treatment, all mice underwent Morris water maze testing in a circular pool (1.1 m diameter) filled with water maintained at 22 ± 1 °C and refreshed daily. During the training phase, a hidden platform (10 cm diameter) was submerged 1 cm below the water surface. Starting positions were varied in a counterbalanced manner. Over four days, each mouse underwent five training trials per day from four different starting points presented in a semi-random order. Mice were given 60 s to locate the platform. Upon success, they remained on the platform for 10 s; if unsuccessful, they were guided to the platform and allowed to stay for the same duration. Upon completion of training, spatial memory was evaluated with a 60 s probe trial in which the platform was removed. Mice were allowed to swim freely, and performance was assessed by measuring the time spent in the target quadrant (where the platform had been) and the number of crossings over the former platform location. All trials were recorded and analyzed using the SuperMaze video tracking system (Shanghai Xinruan Information Technology Co., Ltd., China).

Preparation of the tissue slice and staining

After completing the MWM test, the mice were euthanized through an isoflurane overdose. The tissue sections in the coronal plane were cut at a 40 μm thickness using a freezing sliding microtome, spanning from the genu of the corpus callosum to the caudal extent of the hippocampus (3 μm thick, three sections/mouse, four mice/group). Half of the sections from the neurons were stained with toluidine blue for Nissl body staining. The sections were examined and photographed under a microscope (Hamamatsu, Nano Zoomer). The number of stained cells was counted at 400× magnification in a blinded manner, and only structures of appropriate size and shape were clearly demonstrated. The results are shown as the mean ± s.e.m. ($n = 7$). To evaluate the systemic toxicity of **4b**, the corresponding tissues were collected and sliced, followed by H&E staining according to the reported protocol.

Modeling Tyr-O-glycosylation in Rosetta

In Rosetta, we considered the whole glycosylated Tyr as a non-canonical amino acid (NCAA). Firstly, we combined the glycosylation with Tyr to form 6 new non-canonical residue types, and performed the optimization under B3LYP/6-311G(d) in implicit solvent model with GD3BJ empirical dispersion. The optimized structures of glycosylated Tyr were introduced to Rosetta as Renfrew et al described[77], which enabled us to utilize MutateResidue Mover in RosettaScripts[46] to add glycans on Tyr. Finally, we used PyMOL to truncate and build a 10-layer structure of $A\beta_{42}$–unmodified $A\beta_{9\text{-}21}$ complex, and add various glycans to every glycosylated Tyr on $A\beta_{9\text{-}21}$.

Parameterizing Tyr-O-glycosylation in Gromacs

In Gromacs, we also combined the glycosylation with Tyr to form 6 new non-canonical residue topology files in Gromacs. These non-canonical residues were parameterized with restrained electrostatic potential (RESP) charges[78] using Gaussian 16[79], Antechamber[80], and ACPYPE[81].

We obtained the force field parameters for these glycosylated tyrosine from Amber14SB[47] (for the tyrosine part) and GLYCAM06[45] (for the glycans part). For the parameters of tyrosine glycosidic bonds, we refer to the force field parameters of serine glycosylation.

MD simulation settings

All simulations were performed using Gromacs 2020.1 version[82]. Amber14SB force field was used to treat the system excluding the glycosylated tyrosine. Every system was solvated in a cubic box with 12 Å distance between the solute and the box and 50 mM of NaCl. Steep descent (SD) method was chosen to carry out energy minimization. Then, the periodic box system was equilibrated to the desired temperature of 300 K (NVT) using velocity rescale thermostat method[83] with coupling time constant (τ_T) of 0.1 ps, followed by an 1 ns MD simulation in an NPT ensemble at 1.0 bar using Parrinello-Rahman barostat[84] with coupling time constant (τ_T) of 0.2 ps. Finally, the production MD runs were carried out for all the systems for 100 ns. The complete procedures were repeated twice for reproducibility with different random seeds. For all kinds of electrostatics, particle-mesh Ewald (PME) method[85] was used with 0.9 nm cutoff in real-space, and van der Waals interaction was also cut off at 0.9 nm with long-range dispersion correction. The LINCS algorithm[86] was implemented to constrain all bonds involving hydrogen (h-bonds) with time step of 2 fs. Analysis of backbone RMSD revealed that the complexes reached equilibrium around 10 ns, and thus the following 90 ns were used for detailed analysis. All the structure figures were drawn with PyMOL.

Reporting summary

Further information on research design is available in the Nature Portfolio Reporting Summary linked to this article.

Data availability

Density maps of $A\beta_{42}$-**4b**-P1, $A\beta_{42}$-**4b**-P2, $A\beta_{42}$-**4b**-P3 and $A\beta_{42}$ WT have been deposited in Electron Microscopy Data Bank (EMDB) under accession codes: EMD-61944, EMD-61945, EMD-61946 and EMD-63403 respectively. The structure models have been deposited in the Protein Data Bank (PDB) with entry codes: 9K0D ($A\beta_{42}$-**4b**-P1), 9K0E ($A\beta_{42}$-**4b**-P2), and 9K0F ($A\beta_{42}$-**4b**-P3). Unless otherwise stated, all data supporting the results of this study can be found in the article, supplementary, and source data files. Source data are provided with this paper.

Code availability

The modeling of glycosylated Tyr was done with RosettaScripts. The method used for parametrizing and the Rosetta params file for six types of glycosylated Tyr can be found in Supplementary information. The Rosetta software suite is available free of charge to academic users and can be downloaded from http://www.rosettacommons.org. The force field of glycosylated Tyr used in Gromacs was from Amber14SB and GLYCAM06.

References

1. Whitesides, G. M. & Grzybowski, B. Self-assembly at all scales. *Science* **295**, 2418–2421 (2002).
2. Chagri, S., Ng, D. Y. & Weil, T. Designing bioresponsive nanomaterials for intracellular self-assembly. *Nat. Rev. Chem.* **6**, 320–338 (2022).
3. Vaquer-Alicea, J. & Diamond, M. I. Propagation of protein aggregation in neurodegenerative diseases. *Annu. Rev. Biochem.* **88**, 785–810 (2019).
4. Lee, S. J. C., Nam, E., Lee, H. J., Savelieff, M. G. & Lim, M. H. Towards an understanding of amyloid-β oligomers: characterization, toxicity mechanisms, and inhibitors. *Chem. Soc. Rev.* **46**, 310–323 (2017).
5. Bates, K. et al. Clearance mechanisms of Alzheimer's amyloid-β peptide: implications for therapeutic design and diagnostic tests. *Mol. Psychiatry* **14**, 469–486 (2009).
6. Wong, Y. C. & Krainc, D. α-synuclein toxicity in neurodegeneration: mechanism and therapeutic strategies. *Nat. Med.* **23**, 1–13 (2017).
7. Paredes-Rosan, C. A., Valencia, D. E., Barazorda-Ccahuana, H. L., Aguilar-Pineda, J. A. & Gómez, B. Amyloid beta oligomers: how pH influences over trimer and pentamer structures?. *J. Mol. Model.* **26**, 1–8 (2020).
8. Kotler, S. A., Walsh, P., Brender, J. R. & Ramamoorthy, A. Differences between amyloid-β aggregation in solution and on the membrane: insights into elucidation of the mechanistic details of Alzheimer's disease. *Chem. Soc. Rev.* **43**, 6692–6700 (2014).
9. Kummer, M. P. & Heneka, M. T. Truncated and modified amyloid-beta species. *Alzheimer's Res. Ther.* **6**, 1–9 (2014).
10. Han, X. & He, G. Toward a rational design to regulate β-amyloid fibrillation for Alzheimer's disease treatment. *ACS Chem. Neurosci.* **9**, 198–210 (2018).
11. Liu, H. et al. Small molecule-mediated co-assembly of amyloid-β oligomers reduces neurotoxicity through promoting non-fibrillar aggregation. *Chem. Sci.* **11**, 7158–7169 (2020).
12. Faridi, A. et al. Mitigating human IAPP amyloidogenesis in vivo with chiral silica nanoribbons. *Small* **14**, 1802825 (2018).
13. Ke, P. C. et al. Mitigation of amyloidosis with nanomaterials. *Adv. Mater.* **32**, 1901690 (2020).
14. Jokar, S. et al. Recent advances in the design and applications of amyloid-β peptide aggregation inhibitors for Alzheimer's disease therapy. *Biophys. Rev.* **11**, 901–925 (2019).
15. Frenkel-Pinter, M. et al. Distinct effects of O-GlcNAcylation and phosphorylation of a tau-derived amyloid peptide on aggregation of the native peptide. *Chemistry A Eur. J.* **24**, 14039–14043 (2018).
16. Ryan, P. et al. O-GlcNAcylation of truncated NAC segment alters peptide-dependent effects on α-synuclein aggregation. *Bioorg. Chem.* **94**, 103389 (2020).
17. Yang, A. et al. Attenuation of β-Amyloid Toxicity In Vitro and In Vivo by Accelerated Aggregation. *Neurosci. Bull.* **33**, 405–412 (2017).
18. Pallitto, M. M., Ghanta, J., Heinzelman, P., Kiessling, L. L. & Murphy, R. M. Recognition sequence design for peptidyl modulators of β-amyloid aggregation and toxicity. *Biochemistry* **38**, 3570–3578 (1999).
19. Kuhn, A. J. et al. Amyloid-α peptide formed through alternative processing of the amyloid precursor protein attenuates Alzheimer's amyloid-β toxicity via cross-chaperoning. *J. Am. Chem. Soc.* **146**, 2634–2645 (2024).
20. Pilkington, E. H. et al. Star polymers reduce islet amyloid polypeptide toxicity via accelerated amyloid aggregation. *Biomacromolecules* **18**, 4249–4260 (2017).
21. Chen, P. et al. Amyloidosis inhibition, a new frontier of the protein corona. *Nano Today* **35**, 100937 (2020).
22. Kayed, R. & Lasagna-Reeves, C. A. Molecular mechanisms of amyloid oligomers toxicity. *J. Alzheimer's Dis.* **33**, S67–S78 (2013).
23. Cline, E. N., Bicca, M. A., Viola, K. L. & Klein, W. L. The amyloid-β oligomer hypothesis: beginning of the third decade. *J. Alzheimer's Dis.* **64**, S567–S610 (2018).
24. Frenkel-Pinter, M. et al. Interplay between protein glycosylation pathways in Alzheimer's disease. *Sci. Adv.* **3**, e1601576 (2017).
25. Liu, D. et al. O-glycosylation induces amyloid-β To form new fibril polymorphs vulnerable for degradation. *J. Am. Chem. Soc.* **143**, 20216–20223 (2021).
26. Hu, J. et al. Phosphorylation and O-GlcNAcylation at the same α-synuclein site generate distinct fibril structures. *Nat. Commun.* **15**, 2677 (2024).
27. Kobayashi, H. et al. Molecular design of "super" hydrogelators: understanding the gelation process of azobenzene-based sugar derivatives in water. *Org. Lett.* **4**, 1423–1426 (2002).

28. He, C. et al. Glycopeptide self-assembly modulated by glycan stereochemistry through glycan–aromatic interactions. *J. Am. Chem. Soc.* **142**, 17015–17023 (2020).
29. Petkova, A. T. et al. A structural model for Alzheimer's β-amyloid fibrils based on experimental constraints from solid state NMR. *Proc. Natl. Acad. Sci. USA* **99**, 16742–16747 (2002).
30. Armiento, V., Spanopoulou, A. & Kapurniotu, A. Peptide-based molecular strategies to interfere with protein misfolding, aggregation, and cell degeneration. *Angew. Chem. Int. Ed.* **59**, 3372–3384 (2020).
31. Halim, A. et al. Site-specific characterization of threonine, serine, and tyrosine glycosylations of amyloid precursor protein/amyloid β-peptides in human cerebrospinal fluid. *Proc. Natl. Acad. Sci. USA* **108**, 11848–11853 (2011).
32. Ban, T., Hamada, D., Hasegawa, K., Naiki, H. & Goto, Y. Direct observation of amyloid fibril growth monitored by thioflavin T fluorescence * 210. *J. Biol. Chem.* **278**, 16462–16465 (2003).
33. Kasim, J. K. et al. Efficient synthesis and characterisation of the amyloid beta peptide, Aβ 1–42, using a double linker system. *Org. Biomol. Chem.* **17**, 30–34 (2019).
34. Meisl, G. et al. Differences in nucleation behavior underlie the contrasting aggregation kinetics of the Aβ40 and Aβ42 peptides. *Proc. Natl. Acad. Sci. USA* **111**, 9384–9389 (2014).
35. Vicidomini, G., Bianchini, P. & Diaspro, A. STED super-resolved microscopy. *Nat. Methods* **15**, 173–182 (2018).
36. Wälti, M. A. et al. Atomic-resolution structure of a disease-relevant Aβ(1–42) amyloid fibril. *Proc. Natl. Acad. Sci.* **113** https://doi.org/10.1073/pnas.1600749113 (2016).
37. Gremer, L. et al. Fibril structure of amyloid-β(1–42) by cryo–electron microscopy. *Science* **358**, 116–119 (2017).
38. Colvin, M. T. et al. Atomic resolution structure of monomorphic Aβ42 amyloid fibrils. *J. Am. Chem. Soc.* **138**, 9663–9674 (2016).
39. Yang, Y. et al. Cryo-EM structures of amyloid-β 42 filaments from human brains. *Science* **375**, 167–172 (2022).
40. Wilkinson, M. et al. Structural evolution of fibril polymorphs during amyloid assembly. *Cell* **186**, 5798–5811.e5726 (2023).
41. Lövestam, S. et al. Disease-specific tau filaments assemble via polymorphic intermediates. *Nature* **625**, 119–125 (2024).
42. Huang, G., Song, Z., Xu, Y., Sun, Y. & Ding, F. Deciphering the morphological difference of Amyloid-β fibrils in familial and sporadic Alzheimer's diseases. *J. Chem. Inf. Model.* **64**, 8024–8033 (2024).
43. Danne et al. doGlycans–Tools for Preparing Carbohydrate Structures for Atomistic Simulations of Glycoproteins, Glycolipids, and Carbohydrate Polymers for GROMACS. *J. Chem. Inf. Model.* **57**, 2401–2406 (2017).
44. Jo, S., Kim, T., Iyer, V. G. & Im, W. CHARMM-GUI: a web-based graphical user interface for CHARMM. *J. Comput. Chem.* **29**, 1859–1865 (2008).
45. Kirschner, K. N. et al. GLYCAM06: a generalizable biomolecular force field. Carbohydrates. *J. Comput. Chem.* **29**, 622–655 (2008).
46. Fleishman, S. J. et al. RosettaScripts: a scripting language interface to the rosetta macromolecular modeling suite. *PLoS ONE* **6**, e20161 (2011).
47. Maier, J. A. et al. ff14SB: improving the accuracy of protein side chain and backbone parameters from ff99SB. *J. Chem. Theory Comput.* **11**, 3696–3713 (2015).
48. Wang, J., Wolf, R. M., Caldwell, J. W., Kollman, P. A. & Case, D. A. Development and testing of a general amber force field. *J. Comput. Chem.* **25**, 1157–1174 (2004).
49. Merz, G. E. et al. Stacked binding of a PET ligand to Alzheimer's tau paired helical filaments. *Nat. Commun.* **14**, 3048 (2023).
50. Hefti, F. et al. The case for soluble Aβ oligomers as a drug target in Alzheimer's disease. *Trends Pharmacol. Sci.* **34**, 261–266 (2013).
51. Benilova, I., Karran, E. & De Strooper, B. The toxic Aβ oligomer and Alzheimer's disease: an emperor in need of clothes. *Nat. Neurosci.* **15**, 349–357 (2012).
52. Xie, R. et al. In vivo metabolic labeling of sialoglycans in the mouse brain by using a liposome-assisted bioorthogonal reporter strategy. *Proc. Natl. Acad. Sci. USA* **113**, 5173–5178 (2016).
53. Baker-Nigh, A. et al. Neuronal amyloid-β accumulation within cholinergic basal forebrain in ageing and Alzheimer's disease. *Brain* **138**, 1722–1737 (2015).
54. Wu, J. W. et al. Neuronal activity enhances tau propagation and tau pathology in vivo. *Nat. Neurosci.* **19**, 1085–1092 (2016).
55. Horsley, J. R. et al. Rationally designed peptide-based inhibitor of Aβ42 fibril formation and toxicity: a potential therapeutic strategy for Alzheimer's disease. *Biochem. J.* **477**, 2039–2054 (2020).
56. Jokar, S. et al. Design of peptide-based inhibitor agent against amyloid-β aggregation: molecular docking, synthesis and in vitro evaluation. *Bioorg. Chem.* **102**, 104050 (2020).
57. Li, X., Du, Y., Chen, X. & Liu, C. Emerging roles of O-glycosylation in regulating protein aggregation, phase separation, and functions. *Curr. Opin. Chem. Biol.* **75**, 102314 (2023).
58. Lv, P. et al. O-GlcNAcylation modulates liquid–liquid phase separation of SynGAP/PSD-95. *Nat. Chem.* **14**, 831–840 (2022).
59. Levine, P. M. et al. α-Synuclein O-GlcNAcylation alters aggregation and toxicity, revealing certain residues as potential inhibitors of Parkinson's disease. *Proc. Natl. Acad. Sci. USA* **116**, 1511–1519 (2019).
60. Limbocker, R. et al. Trodusquemine enhances Abeta42 aggregation but suppresses its toxicity by displacing oligomers from cell membranes. *Nat. Commun.* **10**, 225 (2019).
61. Doig, A. J. & Derreumaux, P. Inhibition of protein aggregation and amyloid formation by small molecules. *Curr. Opin. Struct. Biol.* **30**, 50–56 (2015).
62. Viola, K. L. & Klein, W. L. Amyloid β oligomers in Alzheimer's disease pathogenesis, treatment, and diagnosis. *Acta Neuropathol.* **129**, 183–206 (2015).
63. Muttenthaler, M., King, G. F., Adams, D. J. & Alewood, P. F. Trends in peptide drug discovery. *Nat. Rev. Drug Discov.* **20**, 309–325 (2021).
64. Xia, L. et al. Development of a GalNAc-tyrosine-specific monoclonal antibody and detection of tyrosine O-GalNAcylation in numerous human tissues and cell lines. *J. Am. Chem. Soc.* **144**, 16410–16422 (2022).
65. Behren, S., Schorlemer, M., Schmidt, G., Aktories, K. & Westerlind, U. Antibodies directed against GalNAc- and GlcNAc-O-tyrosine posttranslational modifications – a new tool for glycoproteomic detection. *Chem. A Eur. J.* **29**, e202300392 (2023).
66. Javed, I. et al. Accelerated amyloid beta pathogenesis by bacterial amyloid FapC. *Adv. Sci.* **7**, 2001299 (2020).
67. Micsonai, A. et al. BeStSel: a web server for accurate protein secondary structure prediction and fold recognition from the circular dichroism spectra. *Nucleic Acids Res.* **46**, W315–W322 (2018).
68. Zheng, S. Q. et al. MotionCor2: anisotropic correction of beam-induced motion for improved cryo-electron microscopy. *Nat. Methods* **14**, 331–332 (2017).
69. Rohou, A. & Grigorieff, N. CTFFIND4: Fast and accurate defocus estimation from electron micrographs. *J. Struct. Biol.* **192**, 216–221 (2015).
70. Scheres, S. H. W. RELION: implementation of a Bayesian approach to cryo-EM structure determination. *J. Struct. Biol.* **180**, 519–530 (2012).
71. He, S. & Scheres, S. H. W. Helical reconstruction in RELION. *J. Struct. Biol.* **198**, 163–176 (2017).
72. Zivanov, J. et al. New tools for automated high-resolution cryo-EM structure determination in RELION-3. *Elife* **7** https://doi.org/10.7554/eLife.42166 (2018).
73. Emsley, P., Lohkamp, B., Scott, W. G. & Cowtan, K. Features and development of Coot. *Acta Crystallogr D. Biol. Crystallogr* **66**, 486–501 (2010).

74. Adams, P. D. et al. PHENIX: a comprehensive Python-based system for macromolecular structure solution. *Acta Crystallogr D. Biol. Crystallogr* **66**, 213–221 (2010).
75. Afonine, P. V. et al. Real-space refinement in PHENIX for cryo-EM and crystallography. *Acta Crystallogr D. Struct. Biol.* **74**, 531–544 (2018).
76. Sun, J. et al. Metabolic glycan labeling in primary neurons enabled by unnatural sugars with no S-glyco-modification. *ACS Chem. Biol.* **18**, 1416–1424 (2023).
77. Renfrew, P. D., Choi, E. J., Bonneau, R. & Kuhlman, B. Incorporation of noncanonical amino acids into Rosetta and use in computational protein-peptide interface design. *PLoS One* **7**, e32637 (2012).
78. Bayly, C. I., Cieplak, P., Cornell, W. & Kollman, P. A. A well-behaved electrostatic potential based method using charge restraints for deriving atomic charges: the RESP model. *J. Phys. Chem.* **97**, 10269–10280 (1993).
79. Gaussian 16 Rev. C.01 (Wallingford, 2016).
80. Wang, J., Wang, W., Kollman, P. A. & Case, D. A. Automatic atom type and bond type perception in molecular mechanical calculations. *J. Mol. Graph Model.* **25**, 247–260 (2006).
81. Sousa da Silva, A. W. & Vranken, W. F. ACPYPE - AnteChamber PYthon Parser interface. *BMC Res. Notes* **5**, 367 (2012).
82. Abraham, M. J. et al. GROMACS: high performance molecular simulations through multi-level parallelism from laptops to supercomputers. *SoftwareX* **1-2**, 19–25 (2015).
83. Bussi, G., Donadio, D. & Parrinello, M. Canonical sampling through velocity rescaling. *J. Chem. Phys.* **126**, 014101 (2007).
84. Martonák, R., Laio, A. & Parrinello, M. Predicting crystal structures: the Parrinello-Rahman method revisited. *Phys. Rev. Lett.* **90**, 075503 (2003).
85. Darden, T., York, D. & Pedersen, L. Particle mesh Ewald: an N·log(N) method for Ewald sums in large systems. *J. Chem. Phys.* **98**, 10089–10092 (1993).
86. Hess, B., Bekker, H., Berendsen, H. J. C. & Fraaije, J. G. E. M. LINCS: A linear constraint solver for molecular simulations. *J. Comput. Chem.* **18**, 1463–1472 (1997).

Acknowledgements

The authors are grateful for financial support from the National Natural Science Foundation of China (22321005 and 92153301 to S.D. and C.W.; 22425704 and 82188101 to C.L.), National Key R&D Program of China (2022YFA1300008 to Y.L.), AI4S interdisciplinary program from Peking University to C.W., the Strategic Priority Research Program of the Chinese Academy of Sciences (XDB1060000 to C.L.), Shanghai Basic Research Pioneer Project to C.L., Shanghai Municipal Science and Technology Major Project to C.L. and the State Key Laboratory of Natural and Biomimetic Drugs. Professor Cong Liu is a SANS Exploration Scholar. We thank Dr. Wei Li and Professor Xing Chen (Peking University) for experimental assistance and helpful discussion on liposome preparation, Dr. Shiyong Cui, Yufei Hu and Professor Jing Wang (Peking University) for experimental assistance on primary neuron preparation, Drs. Yuan Wang and Xiaohui Zhang (Peking University) for spectroscopic assistance, the Cryo-Electron Microscopy Center at Interdisciplinary Research Center on Biology and Chemistry (Shanghai Institute of Organic Chemistry) for help with data collection and Xingyue Yang (Peking University) for assistance on image creation. BioRender.com was used in generating Fig. 7b.

Author contributions

S.D., C.L. and Y.L. conceptualized and supervised the study. Q.W. and D.L. synthesized the peptides and performed the characterization. W.X. conducted cryo-EM data collection and analysis with assistance from Z.X. F.W. carried out molecular dynamics simulations with input from C.W. L.H. performed UPLC-MS quantification and cell assay. Q.W. and D.L. conducted animal experiments with assistance from L.H., J.Z. and X.W. C.H. contributed to the synthesis of building blocks. W.L. contributed to high-resolution imaging and X.S. contributed to MS and structural analysis. Q.W., D.L., W.X., F.W., Y.L., C.L. and S.D. wrote the manuscript with input from all authors. All authors contributed to data analysis and interpretation.

Competing interests

The authors declare no competing interests.

Additional information

Supplementary information The online version contains supplementary material available at https://doi.org/10.1038/s41467-025-60978-w.

Correspondence and requests for materials should be addressed to Yuan Liu, Cong Liu or Suwei Dong.

Peer review information *Nature Communications* thanks Iva Pashkuleva and the other, anonymous, reviewer(s) for their contribution to the peer review of this work. A peer review file is available.